RECEIVED
LAWRENCE
BERKELEY LABORATORY

JUN 14 1978

LIBRARY AND
DOCUMENTS SECTION

LBL-7638
c.2

PORE STRUCTURE AND GROWTH KINETICS IN CARBON MATERIALS

Sudhangshu Bose
(Ph. D. thesis)

April 1978

Prepared for the U. S. Department of Energy
under Contract W-7405-ENG-48

TWO-WEEK LOAN COPY

This is a Library Circulating Copy which may be borrowed for two weeks. For a personal retention copy, call Tech. Info. Division, Ext. 6782

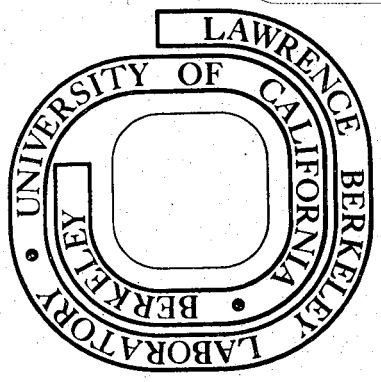

LBL-7638
c.2

This report was done with support from the Department of Energy. Any conclusions or opinions expressed in this report represent solely those of the author(s) and not necessarily those of The Regents of the University of California, the Lawrence Berkeley Laboratory or the Department of Energy.

TABLE OF CONTENTS

ABSTRACT v

ACKNOWLEDGMENTS x

1. INTRODUCTION 1

2. GLASSY CARBON 3

I. REVIEW 3

A. Historical 3

B. Structure of Carbon 4

C. Structure of Glassy Carbon 5

D. Graphitization 8

II. SAMPLE PREPARATION 10

A. Material 10

B. Heat Treatment 10

III. MICROSTRUCTURE 12

A. Transmission Electron Microscopy 12

B. XRD Work 13

IV PORE STRUCTURE 15

A. Introduction 15

B. Density Measurements 16

C. Small Angle X-ray Scattering 18

3. PYROLYTIC GRAPHITE 28

I. REVIEW 28

A. Historical 28

B. Microstructure 29

C. Theory 30

II. PORE STRUCTURE 31

A. Introduction 31

B. Theory 31

C. Material 35

D. Experimental 35

E. Results and Discussion 36

REFERENCES 40

FIGURE CAPTIONS 45

FIGURES AND TABLES 47-74

PORE STRUCTURE AND GROWTH KINETICS IN CARBON MATERIALS

Sudhangshu Bose

Materials and Molecular Research Division, Lawrence Berkeley Laboratory
and Department of Materials Science and Mineral Engineering
University of California, Berkeley, California 94720

ABSTRACT

Pore structure of glassy carbon (GC) and pyrolytic graphite (PG) have been investigated. GC is one of the most impervious of solids finding applications in prosthetic devices and fuel cells while PG is used extensively in the aerospace industry. One third of the microstructure of GC consists of closed pores inaccessible to fluids. The microstructure of this materials has been characterized using x-ray diffraction (XRD) and high resolution electron microscopy. Small angle x-ray scattering (SAXS) has been used to measure the angstrom sized pores and to follow the evolution of pore surface area as a function of heat treatment temperature (HTT) and heat treatment time (HTt) at constant temperature. From these measurements an analysis of the surface area kinetics was made to find out if rate processes are involved and to locate graphitization occurring at pore surfaces. PG on the other hand has been found to have larger sized pores that comprise five percent of its volume. In addition to being closed these pores are oriented. Some pore models are proposed for PG and the existing scattering theory from oriented ellipsoids is

modified to include the proposed shapes.

The XRD line profiles of GC were very different from those of crystalline materials. High resolution electron microscopic lattice images taken using interference between direct rays and rays reflected by the layers showed fringes parallel to the layer planes. The density of GC was measured as a function of HTt at predetermined HTT. GC was found to give extensive SAXS which arose from angstrom sized pores. Part of the theory of SAXS dealing with nature of interfaces was developed.

PG is a well characterized material whose pore structure was not known because the pores were impermeable to fluids. SAXS theory developed with the help of new models has been applied to the pore structure in PG.

In GC the pores, found to have sharp edges, are shown to belong to two groups, one having layer planes forming the pore walls while the other has pores in the layer planes. It is the latter group that accounts for the coarsening of pores leading to most of the surface area reduction with very limited graphitization. The activation energy of the coarsening process determined from SAXS data agree very well with a vacancy migration mechanism. The density of GC has been found to be constant independent of HTt as long as HTT was kept constant, showing that pore volume did not vary with HTt. This is consistent with a pore coarsening mechanism. The decrease in density with increase in HTT is a composite effect of pressure of pyrolysis gases trapped in pores and rupture of pore edges because of thermal stresses generated by anisotropic thermal expansion.

In PG the scattering data indicated that pores are either ellipsoidal or composites of half ellipsoids. The latter one is more consistent with the variation of interlayer separation in PG as a function of distance from substrate. From the scattering data pore parameters have been determined. The circular and elliptical symmetry observed in the two dimensional scattering pattern have been found to be consistent with all the models of the oriented pores. It is concluded that scattering data alone can not identify the actual model and one has to take recourse to other facts to arrive at the correct pore geometry.

Dedicated in appreciation to my father
Radha Govinda Bose

and with love to my son
Krishnangshu Bose

.....That mystery which lies behind the expressed, is the object of his (scientific man) questioning also; and he, in his scientific way, attempts to render its obtrusive discoveries into human speech. .....

Sir Jagadish Ch. Bose

ACKNOWLEDGMENTS

Professor Robert H. Bragg introduced the author to the wonderful realm of carbons. He has provided constant guidance and encouragment throughout the present investigation. With profound gratitude I acknowledge my indebtedness to him. I am also indebted to the Materials and Molecular Research Division of the Lawrence Berkeley Laboratory for financial support and a research assistantship. The Department of Materials Science and Mineral Engineering, University of California, Berkeley was gracious enough to provide me with two quarters of teaching assistantship and a readership.

My friends and associates helped shape up this presentation. I am especially thankful to my fellow student Ulrich Dahman for the lattice image, support staff Jack Wodei for mending the often unruly x-ray machines, Gloria Pelatowski for her beautifully professional drawings, and John Walsh and his colleagues for setting up the furnace. Lois Fernander and Carmen Hubbard carefully and patiently typed the manuscript. My gratitude to them.

Professor Alan Searcy of the Materials Science and Mineral Engineering Department spent much of his valuable time and shared his ideas that helped me form the pore coarsening model of glassy carbon. It is a pleasure to acknowledge his help. I am indebted to Professor Charles Kittel of Physics and Professor Jack Washburn of Materials Science for serving on the Thesis Committee.

My parents and especially my sister Mridula have always been a source of great strength behind my endeavours. I fondly acknowledge their support.

Finally my deepest love and appreciation to my wife Juthi. She has been a constant source of inspiration through the years. The story in the following pages is a result of the innumerable sacrifices she made to see me succeed.

Work supported by the U. S. Department of Energy.

1. INTRODUCTION

Graphite is the stable, thermodynamic equillibrium cyrstalline form of solid element carbon at ordinary pressures. However, carbon can and does exist metastably in other crystallographically ordered forms such as diamond and a wide range of disordered or imperfectly ordered structures.

A group of these carbons transform to graphite on heating to or below 3000^{o}C. They are termed "graphitizable" carbons. The other group called "non-graphitizable" do not become graphite even on heating to 3000^{o}C. The difference between these two groups of carbon is much more profound than their crystallographic c-parameter indicate. In this work an endeavour has been made to study the closed pore structure in the two groups of carbons.

Glassy carbon (GC) has been chosen as a representative of the nongraphitizable class because it hardly graphitizes, is reproducible in microstructure and properties, and holds great technological promise in applications such as prosthetic devices, energy storage systems and high temperature ceramics. GC has slit shaped closed pores that are inaccessible by molecular means of conventional porosimetry. It has been fairly established that a considerable fraction of the "graphitization" that GC undergoes occurs around pores which are introduced artifically by sintering. In the present work techniques have therefore been used which could probe the immediate vicinity of the inherently present

submicroscopic pores. The microstructure of GC was characterized and the pore structure investigated. The kinetics of pore evolution on heat treatment is analyzed to arrive at an activation energy. A possible mechanism of the evolution is outlined.

The representative of graphitizable carbon chosen is pyrolytic carbon, often called pyrolytic graphite (PG). PG has already established itself as a material for numerous technological applications in aerospace, nuclear and other fields. The pores in PG are oriented and have been interpreted in terms of a theory of scattering by oriented ellipsoids. A more realistic model of the pore geometry in PG is proposed and the existing theory is modified accordingly. The pores in PG provide an ideal vehicle to test the theory which could profitably be used eventually to characterize oriented inhomogeneities in other materials systems such as elongated phases in spinodal systems decomposed in the presence of magnetic or stress fields.

2. GLASSY CARBON

I. REVIEW

A. Historical

An area of interest in the carbon field has been the production of disordered carbons starting with thermosetting polymeric resins. These materials are termed "glassy carbon" (GC) mainly because they are black, shiny, brittle solids that break with concoidal fracture. The main objective of producing glassy carbon was to develop a material which is impermeable to gases and liquids. It is different from other forms of carbon in that even on a microscopic scale it is isotropic owing to its tangled, lath-like microstructure with very small apparent crystallite size. However, contrary to the behavior of other forms of carbon, GC hardly graphitizes, even on heat treatment to $3000^{o}C$. Some of the properties of GC vis-a-vis those of graphite and diamond are listed in Table 1. Several processes for the commercial production of glass-like carbon are available now. These are reviwed in outline by Noda et al., (1) and in detail by Jenkins and Kawamura (2). Thermosetting resins e.g., phenolformaldehyde, furfuryl alcohol, divinyl benzene, furfural benzaldehyde and napthalenediol polymerized in the presence of catalysts such as ammonium hydroxide or p-toluene suphonic acid have been used as precursors. They are cured, carbonized very slowly and then heated at elevated temperatures. The structure produced contains a significant volume of closed voids, about 30 percent. The material is a cavy aperture system. An integral part

of the microstructure, these cavities or voids play a very important role in the structure evolution of glassy carbon on heat treatment.

B. Structure of Carbon

The carbon atom has four orbitals in the valence shell; one 2s orbital with a bond strength of unity and three 2p orbitals with a bond strength of 1.732. Pauling (3) has shown that if the four bonds are assumed to be equivalent and directed toward the corners of a regular tetrahedron, then sp^3 or tetrahedral bond will have a strength of 2. If on the other hand each atom has three strong bonds at 120^o to each other, trigonal bonds will form with strength 1.605. These are the covalent bonds of diamond and graphite respectively. Cubic diamond has interatomic distance of 1.54Å. The high co-ordination number supported by strong covalent bonds renders diamond the hardest known material with a high density and melting point.

It has been commonly accepted that graphite is made up of layers in which C atoms form trigonal and π bond with three neighboring atoms. The unit cell is hexagonal with 4 atoms per unit cell. The layers are stacked in such a manner that any two pairs alternate i.e. the sequence is A-B-A-B-A. Occasionally a sequence A-B-C-A-B-C-A is encountered, usually on mechanical grinding with a rhombohedral unit cell and 6 atoms per cell. Since this form has never been isolated it is treated more as a stacking disorder than as a separate phase. To explain the apparently low basal plane compressibility in graphite compared to that of diamond Pauling (4) proposed that the layer planes in graphite have a 1-4 quinoid structure. In this structure each carbon atom forms one bond that

has a large amount and the other two smaller amount of double bond character giving the bond lengths 1.453Å (70% double bond character). Bond angle are expected to be 112^{o}, 124^{o} and 124^{o}. Ergun (5) claimed that his data on pyrolytic graphite indicated an apparent quinoid structure in the graphite layer. Later, however, Donohue (6) detected serious error in Ergun's analysis. Neutron and x-ray diffraction studies by Trucano and Chen (7,8) confirmed the classical Bernal structure with the refined C-C distance in plane 1.422 ± 0.001Å and unit cell parameters $a = 2.461$Å, $c = 6.706$Å at 293^{o}K. To date there has been no experimental confirmation of Pauling's quinoidal structure of graphite.

In addition to cubic diamond and hexagonal graphite, carbon has been found to occur in other crystallographic forms. The most interesting of these forms, in recent years, have been the linear carbons called 'Carbynes'.

C. Structure of Glassy Carbon

The structure of GC has been investigated by a number of workers using a variety of techniques (2). But the structure is not well understood. The microstructural development on pyrolysis of resins have been followed by Fitzer et al. (9). They found that the material shrinks on pyrolysis up to 800^{o}C when it reaches almost a constant volume. Micropore volume, BET surface area and water adsorption measurements pass through a maximum around $700-800^{o}$C. Beyond about 1000^{o}C there are no detectable pores left even though the density remains far less than that of graphite. The material produced is featureless when viewed in the optical microscope, SEM (10) and conventional TEM.

The bonding in GC has been the subject of considerable controversy. Ergun and Tiensuu (11) showed that clusters of tetrahedrally bonded carbon atoms give rise to diffraction peaks in the same region where (10) and (11) reflexions of graphite-like structures occur. Noda and Inagaki (12) have analyzed the radial distribution function of GC. They concluded that there are both trigonally and tetrahedrally bonded carbon atoms present in the structure. Furukawa (13) has suggested the presence of an irregular 3-dimensional network that contains trigonal, planar double, triple, conjugated and tetrahedral bonds. Kakinoki (14) favored a model that consisted of two kinds of domains composed either of tetrahedral or trigonal atoms. These domains are, according to him, bound to each other by oxygen bridges. Laser Raman studies of GC have not been conclusive (15, 16). Saxena and Bragg (17) have studied the K-emission band from diamond, pyrolytic graphite (mounted with c-axis parallel to incident radiation) and three samples of GC heat treated at 1000, 1800 and 2800 for 1 hr each. They observed that the peak x-ray wavelengths of GC lies between those of diamond and pyrolytic graphite. It was concluded that GC contain both trigonal and tetrahedral bonds.

Ergun and Schehl (18) used Fourier transform technique to analyze the GC structure. They found that stacking of layers is extensive but faulty and that the hexagonal rings were distorted. Rousseaux and Tchoubar (19, 20) have studied the structural evolution of GC as a result of thermal treatment between 1000^{o} and 2700^{o}C using XRD and lattice imaging. They claim that the layer diameters in GC are actually larger than the scattering domains obtained by XRD analysis and that the

growth of scattering domains occurs in a direction perpendicular to the primary carbon chains produced from the carbonization of polymer chains.

Oberlin and Rousseaux (21) believe that all hard carbons are composed of three phases when they are heated above 2000°C; non-graphitizable carbon, graphitizable carbon and graphite. Whittaker and Tooper (22) have reported observation of single crystal diffraction patterns of various crystallographic forms of carbon in fragmented GC. They proposed yet another model of GC in which carbon is bonded in all its possible crystalline forms like graphite, diamond, Lonsdaleite, chaotite, carbon IV etc. Similar observations were made by Kaae (23) in selected area electron diffraction patterns of GC. However, unlike those of Whittaker and Tooper, Kaae's samples were made by ion-thinning. A specimen mechanically thinned initially to about one mil in thickness was further thinned bombarding it with 6 keV Argon ions until the specimen was perforated. Kaae could not index the electron diffraction patterns completely because many spacings of forms like chaotite were missing. According to him most of the single crystal inclusions had crystalline turbostratic regions in their vicinity. Saxena and Bragg (24) also reported observing single crystal spot patterns of GC using specimen prepared by crushing. They contend that the spot patterns arise from the diffraction at relatively defect free regions freed by the removal of strain on grinding.

D. Graphitization

Kinetics of graphitization has been reviewed in detail by Fischbach (25) and Pacault (26). Graphitization of 'soft' or graphitizable carbons now seem to be accepted as a thermally activated transformation. The work of Saxena and Bragg (24) on the kinetics of graphitization of GC seems to be the first comprehensive report for this material. Interlayer separation and crystallite size were used to characterize the changes induced by thermal treatments. The activation energy of the transformation is found comparable to that for graphitizable carbons. The resistance to graphitization in GC is attributed to the thermodynamics of the GC $\rightleftharpoons$ graphite transformation. The free energy change associated with this reaction is rather small and Das and Huckle (27) have even found it to be positive for some cases.

One of the most important aspects of graphitization of GC has been the part played by porosity. While studying galvanometric properties of GC Yamaguchi (28) observed that two samples, one dense and impermeable to gas, and the other porous, showed different graphitizability. He was of the opinion that not only did the porous GC graphitize more but its graphitization was non-homogeneous. Kawamura and Tsuzuku (29) used sintering to produce GC with varying amounts of macroscopic porosity. Since "magnetoresistance is a physical quantity independent of porosity", they measured magnetoresistance of GC samples, all heat treated at 2700°C. If all the samples had graphitized to the same extent, magnetoresistance should have remained constant. However, it was observed to increases with increased porosity until at a certain porosity it reached a maximum. Porosity was therefore thought to enhance graphitization. Another

interesting study of the effect of porosity on graphitizability is available in the work of Kamiya and Suzuki (30). Two samples of GC were made from phenol-formaldehyde resin. One was relatively more porous than the other with average pore size of 100 μ. After heat treatment to various temperatures between 1600°C and 2700°C in nitrogen gas, x-ray diffraction patterns were taken. The porous carbon seemed to develop more prominent graphitic components in the x-ray diffraction, (XRD) lines of the samples. Polarized light microscopy indicated that the graphite layers are preferentially aligned around pores.

In addition to the effect of porosity, the effect of pressure on graphitization of GC has also been investigated by a number of workers. Noda and Kato (31) found that in the case of GC a graphitic material with c = 6.72Å was obtained after heat treatment at 2500°C under 10 Kbars pressure. This value of c has never been achieved by heat treating GC even above 3000°C under atmospheric pressure. Chard et al. (32) found in GC sintered at 2700°C that the contacts between angular particles were frequently associated with areas of intense optical anisotropy. They contend that the contact regions had been the sites of strain and plastic deformation during sintering and the localized stress was responsible for graphitization. A similar explanation has been put forward by Kawamura and Tsuzuku (29).

II. SAMPLE PREPARATION

A. Material

GC samples available from Tokai (Japan). Beckwith, Lockheed Missiles and Space Company (LMSC) and Polycarbon, Inc. were examined under SEM (10) to determine the homogeneity and absence of large voids. Beckwith GC had many large pores. Its physical properties indicated that Beckwith GC had inferior mechanical properties. Polycarbon GC is made by a process developed at LMSC. This GC was found to be the most reproducible in terms of measured properties.

Plates of GC of size 8" X 2" X 1/16" were bought from Polycarbon, Inc., North Hollywood. These plates were cut with a diamond saw into small pieces 2" X 1" X 1/16". The materials received from the manufactures were already heat treated at 1000°C for 1 hr. For x-ray, TEM and pore growth studies these pieces were heat treated at selected temperatures for various lengths of time.

B. Heat Treatment

Part of the heat treatment was done in a Pereny furnace with large heat capacity, with a power supply of 20 kva, and the rest in a small Astro furnace (Model 1000-2560-PP20) using a power supply of 12 kva. Both the furnaces used graphite resistance elements. The space between the heating element and the wall of both the furnaces was filled with insulating carbon black. GC samples were then placed in graphite crucibles. In the Pereny furnace the crucible was rested on a PG disc that was screwed on to a graphite rod, the whole assembly in turn being

screwed to the bottom of the furnace. The graphite heating element was a cylinder with the top and the bottom ends thicker than the rest. In the Astro furnace, however, the crucible was placed on a graphite cylinder which rested on the carbon insulating block at the bottom end. The heating element had slots made in it to accommodate thermal expansion and the resulting stresses. A Leeds and Northrup optical pyrometer (catalogue number 8622) calibrated in the temperature range 1000^{o}-3000^{o}C was used to measure temperature. Above 2000^{o}C the precision was $\pm$ 20^{o}C. While the temperature control in the Pereny furnace was automatic, for the Astro furnace prior calibration curves were made to control the temperature manually. Before heating the furnaces, they were purged with a 5 cf/hr flow of Argon gas for about 10 minutes. During heating the flow was reduced to a steady 1 cf/hr for the Pereny and 0.1 cf/hr for the Astro furnace. Water circulation with a flow of 2 gals/min was maintained to cool the metal casings of the furnaces. In case of water loss, both furnaces had intelocks to shut them off. The heating rate was between 70^{o}C/min and 100^{o}C/min.

III. MICROSTRUCTURE

A. Transmission Electron Microscopy

1. Sample preparation and lattice image: GC heat treated at 2700°C for 10 hrs was ground to a thickness of 2 mils. A 2mm disk was then cut ultrasonically. This disk was mounted in an ion-mill where Ar ions impinged on it at 5 keV. In about 100 hrs the disk was perforated at the center giving a thin wedge shaped region suitable for electron microscopy. It was examined in an electron microscope (Philips EM 301) operated at 100 kV. In the phase contrast mode an aperture allowed imaging in the two beam (00.0 - 00.2) situation.

The image formation in an electron microscope is discussed by Cowley (33). The technique and the underlying theory have been reviewed briefly by Gronsky (34). Using the two beam technique we obtained over large thin areas lattice fringes corresponding to the (00.2) planes of graphite. Micrographs were taken slightly under focus.

2. Results and discussion: The selected area diffraction pattern is shown in Fig. 1. Reflexions of the type (hk.l) ($h,k \neq 0$) are absent. This is a consequence of the turbostractic nature of the stacking of layers in GC. The diffraction pattern consists of broad and relatively continuous rings. No single crystal spot patterns were detected.

The lattice image in Fig. 2 shows fringes with no overall preferred orientation indicative of the isotropic nature of GC. The fringe pattern resembled the "Jenkins nightmare" model (35) shown in the inset. The layers show extensive bending, Fig. 3, and stacking disorders are

encountered at places. The thickness of each packet of layers and the distance of continuity of the fringes parallel to the layers correspond to the two crystallite sizes L_a and L_c respectively. The layer spacing was 3.4Å for the specimen used, while the crystallite sizes were roughly $L_a \sim 50$ Å, $L_c \sim 20$ Å in good agreement with XRD measurements.

In conclusion, high resolution electron microscopy has clearly shown that glassy carbon is not in fact amorphous. Our conclusions agree well with those of Ban and Hess (36), Jenkins et al. (35) and Philips (37). Our work on lattice image has been accepted for publication in J. Amer. Ceram. Soc., January 1978. A preprint is available as LBL Report (38).

B. XRD Work

Unlike that of crystalline materials the XRD line profile of GC is characterized by broad and diffuse peaks. Typical raw data, taken on a GE XRD 3 diffractometer using CuK_α radiation and 2^o source, HR Soller and 0.1^o detector slits, and pulse height discriminator is shown in Fig. 4. The detector was a scintillation counter. Goniometer speed was 2^o 2θ/min, chart speed was 1"/min and time constant of the electronics was 0.5 sec. The characteristics of the XRD pattern is that the first peak is asymmetric, the background intensity is fairly high and some of the peaks are so close to each other that they form the so-called (hk) band. To derive meaningful structural and microstructural parameters from such an XRD pattern a standardized procedure was developed (39). Among the corrections to be effected are removal of the low angle scattering intensity whose logarithm was found to be proportional to some negative

power of $\sin\theta$, the background, the geometrical factor, the angular variation of atomic scattering factor and specimen absorption. The corrected profile shown in Fig. 5 is the true interference function with effect of strain still present. In the absence of higher order peaks removal of strain broadening was not feasible. Thus the actual crystallite sizes would be slightly larger than what the uncorrected line profile implies. It has been found that without corrections one is likely to overestimate layer separation by 0.06 Å. Whem it is recalled that the range of d(00.2) between completely disordered (3.44A^{o}) and completely ordered (3.35 Å) carbon is 0.09Å, it is clear that highly erroneous conclusions could be reached about "degree of graphitization" of GC material. Typical values for two samples of GC are:

2700^{o}C	d(00.2) = 3.41Å
	L_a = 44.8 Å
	L_c = 21.8 Å
1200^{o}C	d(00.2) = 3.54 Å
	L_a = 26.5Å
	L_c = 11.8Å

These values agree very well with those observed in the lattice image of GC discussed earlier.

IV. PORE STRUCTURE

A. Introduction

Glassy carbon has a low density (~ 1.5 g/cc) compared to that of single crystal graphite (~ 2.25 g/cc). However, their crystallographic parameters i.e., c and a are not significantly different and therefore can not account for the low density of GC. Thus it is obvious that GC must contain a large volume of pores. Such pores were not observable when the pyrolysis of the precursor polymer and subsequent microstructural development was monitored (9). Conventional bright and dark field electron microscopy does not show these pores either. These observations indicate that the pores must be in the size range of a few Å. N_2 condensation studies and BET measurements give negligible volume and surface area. When coupled with very low permeability of Helium gas ($\sim 10^{-9}$ cm^2/sec) these observations indicate that the pores are closed. Lattice image of GC discussed earlier leads us to the same conclusions. The pores arise out of microstructural constaint imposed by the lath-like fibrils of layers during pyrolysis.

The importance of porosity in graphitization has been established (28-30). However, in previous work the pores were introduced artificially so as to make them visible in the optical microscope. The inherently present pores were not amenable to monitoring because of their extremely small sizes.

A practical application of the knowledge of the pore structure in GC would be to open them up by some process thereby producing an extremely activated carbon (surface area ~600 m^2/cm^3) more active than carbon black.

Measurement of density and its changes on heat treatment is the first step in studying these pores.

B. Density Measurements

1. Data. Densities of GC heat treated at several temperature for various lengths of time were measured using room temperature water as the pycnometer fluid, because previous works have shown that density using helium gas a pycnometer fluid was identical, within limits of experimental error, with that determined using water. Figure 6 shows the variation of density at each temperature as a function of heat treatment time (HTt). Figure 7 shows density as a function of heat treatment temperature (HTT) keeping the samples for 10 hrs at each temperature.

2. Results and Discussion. Contrary to the behavior of many other kinds of carbon, the density of GC is seen to decrease as HTT is increased. Thus the pores must be swelling with rise in HTT. However, the kinetic aspect of density shown in Fig. 6 clearly indicates that as long as the HTT is kept constant the total volume of the voids remains constant.

Fischbach and Rorabaugh (40) have also observed a similar trend of the density of GC as a function of HTT. However for some samples heated above 2700^{o}C densification occurred. The increase in porosity below 2700^{o}C was attributed to the deformation due to the pressure of gases generated within the closed pores. Slower heating rates were shown to result in smaller increase in volume presumably because gases had enough time to diffuse out.

A part of the increase in porosity must be due to opening of the pore ends because of anisotropic thermal expansion and consequent stresses developed at these sites. One can make a rough estimate of the thermal stresses at the pore edges by making the assumption that at these sites the interface along which two 'crystallites' are joined is parallel to the layer plane of one and the prism plane of the other. In such an idealized case the thermal strain on heating the material by ΔT is

$$(\alpha_c - \alpha_a)\,\Delta T$$

where α's are the thermal expansion co-efficient in appropriate directions. The corresponding maximum stress will be

$$\sigma = C_{11} \qquad \text{neglecting other terms compared to } C_{11}$$

using

$$C_{11} = 106 \times 10^{11} \quad \text{dynes/cm}^3 \qquad (80)$$

$$\alpha_c = 26.5 \times 10^{-6}/^{\circ}\text{C} \quad \text{at } 2000^{\circ}\text{C} \qquad (81)$$

$$\alpha_a = 1.2 \times 10^{-6}/^{\circ}\text{C} \quad \text{at } 2000^{\circ}\text{C} \qquad (82)$$

$$\sigma \qquad 5 \times 10^{11} \quad \text{dynes/cm}^3$$

This stress is comparable to failure stress of graphite in the presence of 'Grifith flaw' of size ~ 10 Å. Thus thermal stresses will be a significant source of opening of pores resulting in increase in porosity.

C. Small Angle X-Ray Scattering (SAXS)

1. Introduction. SAXS technique was successfully applied by Guinier to study the kinetics of GP zone formation at a time when the technique of TEM had not been invented. SAXS was therefore one of the appropriate techniques to study voids in GC (41, 42) and monitor changes occurring to the pores on heat treatment.

2. Theory. When the periodicity in the electron density distribution in a structure is large compared to the wavelength of incident radiation, detectable SAXS occurs. The basic theory of SAXS is treated by Guinier and Fournet (44).

(a) If $\rho(\bar{u})$ is the electron density at a point $\bar{u}$ in a particle relative to the surrounding matrix, then the SAXS amplitude will be the Fourier transform and the intensity scattered at angle 2θ from a volume V is

$$I(h) = \int_V \int_V \rho(\bar{u})\ \rho(\bar{u} + \bar{r})\ dV_{\bar{u}}\ \exp(i\bar{h}\cdot\bar{r})dV_{\bar{r}}\ .$$

Using Debye's correlation function defined by

$$C(r) = \int_V \rho(\bar{u})\ \rho(\bar{u} + \bar{r})/V \langle \rho^2 \rangle\ dV_{\bar{u}} \qquad (1)$$

one gets

$$I(h) = V \langle \rho^2 \rangle \int C(r) \exp(i\bar{h}\cdot\bar{r})\ dV_r. \qquad (2)$$

For a centro-symmetric particle, Eq. (2) is identical with

$$I(h) = V \langle \rho^2 \rangle \int_0^\infty 4\pi r^2\ C(r)[\text{Sin } hr/hr]\, dr.$$

Some limiting cases of Eq. (2) are:

$h \to 0$ (Guinier region, small angle in SAXS)

$$I(h) = V \langle \rho^2 \rangle \exp(-1/3\ hRg^2) \tag{3}$$

where R_g is the electronic radius of gyration, sometimes called Guinier radius. For an infinitely long and narrow slit collimator (applied to experimental set up mostly used) Eq. (3) remains intact except for a constant factor dependent on R_g.

$h \to \infty$ (Porod region, valid at large angles of SAXS)

$I(h) = 2\pi \langle \rho^2 \rangle S/h^4$ where S is the interface area of the two phase scattering system. For infinitely long and narrow slits this equation reduces to

$$J(h) = \pi^2 \langle \rho^2 \rangle S/h^3. \tag{4}$$

The integrated intensity for slit collimation is

$$\int_0^\infty J(h)\ h\ dh = 4\pi^2 \langle \rho^2 \rangle V c(1-c)$$

where c is the fraction of volume occupied by one phase, say pore in GC. Using Eq. (4) with the last equation one gets an expression for specific surface area S/V:

$$S/V = 4c(1-c)\ \mathrm{Lim} h^3 J(h) / \int_0^\infty hJ(h)dh. \tag{5}$$

(b) The correlation function C(r) has properties similar to those of the Patterson function of crystallography. If one end of a vector $\bar{r}$ is within a particle, then C(r) is the probability that the other end of $\bar{r}$ is

also in the particle. In general, for small values of r, C(r) can be expressed as a power series (43);

$$C(r) = 1 - ar + br^2 + Cr^3 + \cdots$$

where a and b are positive and the coefficients depend on the geometry of the interface. Porod et al. (43) showed that for a smooth (i.e., no abrupt change in curvature interface)

$$b = 0 \text{ and } C = \langle k_1 k_2 \rangle / 12 + \langle k_1 - k_2 \rangle^2 / 32 \; S/4Vc \; (1 - c)$$

where k_1 and k_2 are the mean principal curvature. For a smooth interface $b \neq 0$.

Now referring to Fig. 8, Porod showed that the difference in the areas,

$A_1 - A_2 = 16\pi^2 b$ for slit smeared SAXS. Thus for the case of smooth particles $A_1 \sim A_2$, one expects the profile (a) while for particles with sharp edges and corners, $A_1 > A_2$, one expects a profile like (b). These cases have been verified by Tchoubar and Mering (45) using dilute dispersion of spherules (smooth) of Teflon, cubic crystals (sharp) of MgO and a porous compact (sharp edges of pores) of Teflon.

(c) Equation (4) is valid only when the electron density transition at the interface is sharp. However, there are actual systems where the interface is known to be diffuse. An endeavour is therefore made here to provide a semiquantitative theory to characterize diffuse interfaces using SAXS (46). The content of this theory with experimental verification has been submitted to Met. Trans. (A). Following Hoseman and Bagchi (47)

and Ruland (48) one can represent an electron density with a diffuse interface as the convolution between an electron density of sharp interface and a smoothing function such as a Gaussian. Thus

$$\rho \text{ diff}(\bar{u}) = \int g(\bar{w})\rho(\bar{w} + \bar{u})dV\bar{w} = g(\bar{w}) * \rho(\bar{u})$$

where g(w) is the smoothing function. The new correlation function is given by

$$C_{diff}(r) = \int_V \rho_{diff}(\bar{u})\rho_{diff}(\bar{u} + \bar{r})V \langle\rho^2\rangle \, dV_{\bar{u}} .$$

Upon inserting Eq. (1) into the above equation one obtains the relation

$$C_{diff}(r) = C(r) * g(r^{*2}).$$

Here the subscript diff means "for diffuse interface" and *2 is a self convolution. The intensity equation for the particle with diffuse interface is obtained by taking the Fourier transform of the last equation

$$I_{diff}(h) = I(h) \, [G(h)]^2$$

where G(h) is the Fourier transform of the smoothing function. Thus

$$G(h) = [I_{diff}(h)/I(h)]^{1/2}$$

which is equivalent to

$$\int_V g(w) \exp(i\bar{h}\cdot\bar{w})dV_{\bar{w}} = [I_{diff}(h)/I(h)]^{1/2} .$$

By inverse Fourier transform one is able to determine the smoothing function

$$g(\bar{w}) = (1/2\pi)^3 \int_h [I_{diff}(h)/I(h)]^{-1/2} \exp(-i\bar{h}\cdot\bar{w})dV_{\bar{h}} .$$

A simple approximation is to assume $g(w)$ to be a Gaussian $1/k \exp(-\pi w^2/k)$. Its transform is also a Gaussian $G(h) = \exp(-K^2h^2/4\pi)$. Thus

$$I_{diff}(h) = I(h) \exp(-K^2h^2/2\pi).$$

In the Porod region for $K^2h^2/2\pi < 1$ one can expand the exponential and get

$$I_{diff}(h) = 2\pi\langle\rho^2\rangle S/h^4 - \langle\rho^2\rangle K^2 S/2h^2 .$$

For an infinitely long and narrow slit collimation the last equation reduces to

$$J_{diff}(h) = \pi^2\langle\rho^2\rangle S/h^3 - K^2\pi\langle\rho^2\rangle S/2h$$

thus

$$h^3 J_{diff}(h) = \pi^2\langle\rho^2\rangle S - K^2\pi\langle\rho^2\rangle S\, h^2/2$$

for a diffuse interface and

$$h^3 J(h) = \pi\langle\rho^2\rangle S$$

for a sharp interface.

A plot of $h^3J(h)$ against h^2 will be a straight line of negative slope for diffuse interface and zero slope for sharp interface. These inferences have been verified by the author for spinodally decomposed systems (46).

Ruland (48) studied the case of density fluctions in bulk material. In this case

$$h^3 J(h) = \pi\langle\rho^2\rangle S + (\text{constant})\, h.$$

3. Experimental Setup. The slit arrangements of a GE XRD3 diffractometer were modified. The slit combination are as follows:

Incidnet beam slit 0.4^{o}

HR Soller slit replaced by 0.4^{o} source slit in reverse

Detector slit 0.05^{o}.

This slit arrangement was found to satisfy the condition for infinitely long, narrow collimation.

CuK_{α} radiation was used in conjunction with pulse height analyzer. Data were recorded on chart for 2θ angle between 0.4^{o} and 7^{o}. GC samples were in the form of plates 1" X 2" X 1/16" in transmission geometry. Background corrections were made.

4. Results. Typical Porod plots of GC are shown in Fig. 9 where intensity of SAXS is plotted against the modulus of scattering vector h on a log-log scale. These are similar to the ones obtained by Rothwell (41) and Peret and Ruland (42) except that in the region of large h a slope of -3 is achieved. The rise in intensity at very small angles ($h \sim 2 \times 10^{-2}$ Å^{-1}) is known to be a composite effect of multiple scattering and double Bragg diffraction from the layer type planes of GC. The radius of gyration of the pores (44) was determined from the slope of a graph of Log I against h^2. As indicated in Eq. (3), a straight line is expected whose slope gives the radius of gyration Rg. A typical set of Guinier plots is shown in Fig. 10. The radii of gyration so determined are weighted towards larger pores because it is the larger pores that contribute more intensity in the Guinier region. A more fundamental

quantity which is relatively independent of the size distribution and of the geometry of the pores is the specific surface area of the pore-matrix interface. A determination of this parameter requires both the integrated intensity and the Porod invariant $h^3J(h)$, as is clear from Eq. (5). To determine the invariant for each sample of GC, $h^3J(h)$ was plotted against h^2 shown in Fig. 11. The limiting value was determined from the horizontal portions of the curves. In calculating the integrated intensity there is a considerable chance of error for large h because for $h \sim o$, $hJ(h)$ is very small irrespective of the accuracy of $J(h)$. The procedure followed by Gerold (49) was adopted to improve the accuracy. An intermediate region h_o was chosen from where onwards Porod's Law was valid. Then

$$\int_0^\infty hJ(h)dh = \int_0^{h_0} hJ(h)dh + \int_{h_0}^\infty h\, K/h^3 dh$$

$$= \int_0^{h_0} hJ(h) + \frac{K}{h_0}$$

where K is the Porod invariant determined from Fig. 11. Radius of gyration and specific surface area were calculated for each HTt at various HTT in the range 2000-2700°C. The kinetics of Rg and S/V are shown respectively in Fig. 12 and Fig. 13.

5. Discussion. Figure 11 does not show any maxima characteristic of smooth interfaces. In the light of the discussion in the Theory, Section (b), it is evident, therefore, that the pores in GC have sharp edges and corners. This deduction is consistent with the microstructure

determined from TEM lattice image shown in Fig. 2.

The large angle region of Fig. 11 is horizontal. Thus in the Porod region $h^3J(h)$ is constant. As shown in the Theory, Section (c), this means that there is no detectable density fluctuations on the pore surfaces. For those pores which have their walls formed by the layer planes, a density fluctuation would have meant large variations in layer spacings near the pore.

While radius of gyration kinetics do indicate that rate processes are involved, they could not be analyzed possibly because of the fuzzy meaning associated with Rg when pore shapes are not known. However, the specific surface area kinetics have been found to follow a first order rate law:

$$d/dt(S_t - S_\infty) = - k(S_t - S_\infty)$$

where k is the rate constant and S_t is the specific surface area for HTt = t and HTT = T. One thus obtains

$$S_t = S_\infty + (S_o - S_\infty) \exp(-kt).$$

The rate constant is related to the HTT through the Arhenius equation

$$k = k_o \exp(-\Delta H/RT),$$

ΔH being the activation energy per mole of the associated process. A plot of S_t vs exp(-kt) should be a straight line. By curve fitting the values of k for each HTT were determined as shown in Fig. 14. A plot of lnk against 1/T gave a straight line with a negative slope, Fig. 15, where from the activation energy was determined to be 64 ± 10 Kcal/mole (2.8 ± 0.4 eV).

This activation energy determined for GC pores should be compared with that of rate processes in graphite. Table 2 lists some of the activation energies of graphite and graphitizable carbons. Vacancy migration in the layer plane seems to have an activation energy closest to that observed. Because small pores are available which could both be the source and sinks of vacancies, interstitial migration in the c-axix direction having a similar activation energy seems to be a relatively insignificant mechanism. Any model that is accepted as the predominant activated process leading to the reduction in specific surface area of pores in GC should be capable of explaining the following observations discussed in the earlier sections:

GC undergoes only limited graphitization

Pore surfaces have been shown to graphitize preferentially.

The total pore volume remains constant as long as HTT is kept constant.

The tangled microstructure has its own constraints and does not allow extensive realignment.

A model that could explain these observations is shown in Fig. 16. a and b are pores with the layer planes making the pore walls. The layer planes of graphite have very small surface energy ~100 ergs/sq. cm (56), compared to that of any other planes. Thus the driving force from surface area reduction would be very small. Any reduction in the pore surface area of these types of pores would need a co-ordinated breaking and making of bonds at the pore surfaces. This seems improbable. Thus the pores of geometry a and b are stable. Pores c and d however are in the layer planes going through the stacks. Their surfaces are mostly of

high energy and obviously not constant over the whole surface because of extreme anisotropy of the graphite structure. A large pore c situated at a bend and a small one, d, at a relatively straight portion will have two sources of driving force for surface area reduction. One is the reduction in surface energy and the other is the reduction of strain energy on removing the bent regions of the stack by migration of atoms around c towards the smaller pore d. This is the same as vacancy migration from d towards c, thereby coarsening the larger pore c and shrinking the smaller one d.

In this work no effort is made to determine the relative importance of strain energy vis-a-vis surface energy of pores. The model put forward explains the "graphitization" around pores because here layer extensions are occurring at pore site d. If, however, there are constraints such as another stack f blocking the growth of layer planes or if there is no sink pores nearby, graphitization would be halted. Since the pores of type c and d are outnumbered by those of type a and b, and since there are extensive constraints like f, only limited graphitization occurs. As the total number of vacancies moving out of a pore equals that going into sink pores, the overall pore volume does not change with HTt.

The present method of investigation probes only the regions near the pores and therefore does not observe processes going on in the bulk away from pores. Thus bulk graphitization may have an activation energy different from that observed in this investigation.

3. PYROLYTIC GRAPHITE

I. REVIEW

A. Historical

Pyrolytic graphite (PG) is made by the thermal decomposition of hydrocarbon gases on a heated substrate, usually an electrographitized mandrel heated to a temperature above 1500°C by passage of electric current directly through the substrate. The temperature of the substrate and the pressure as well as the rate of flow of the hydrocarbon gas are adjusted so as to achieve the desired texture and properties of the final product. In a number of investigations on PG it has been observed that its electrical, thermal and mechanical properties are considerably different from those of ordinary graphitized products. For example, the tensile strength along the deposition surface is ten times higher than that of ordinary graphitized products (57). The thermal and electrical conductivities are indicative of large anisotropy. They are higher in a plane parallel to the deposition surface than in a perpendicular plane because the crystallites in PG are highly oriented placing their layer planes parallel to the deposition surface. Most of the interesting physico-chemical properties of PG are, thus, largely dependent on the orientation texture. However, the properties measured parallel to the deposition surface do not show any dependence on direction because of the inherent isotropy parallel to the deposition surface.

B. Microstructure

The two major components of PG microstructure are:

(i) preferred orientation (PO) parameter

(ii) pore parameters.

There has been an extensive investigation of PO i.e., the orientation dependence of structure in PG (58-69). The orientation distribution function $f(w) = I(w)/I(o)$ is determined by measuring the intensity $I(w)$ of an (00.ℓ) diffraction peak (usually 00.2) as a function of the angle w between the diffraction vector and the normal to the deposition surface. Thus $f(w)$ is proportional to the number of crystallites having "orientation" w. It has been shown (58-62, 65) that $f(w)$ can be represented quite well by the function $\text{Cos}^n w$, where the exponent n can be employed as a measure of the degree of PO. Bragg et al. (63,64), however, showed that $f(w)$ is approximately a Gaussian $\exp(-w^2/2\sigma^2)$. σ can be used as a measure of the degree of PO. Fischbach (69) showed that both approaches are equivalent for the range of texture normally encountered. A consequence of the strong PO is the "growth cone" microstructure of PG. The microstructure shows cones originating from nucleation centers. For substrate nucleated PG the cones with their apex at the substrate run all the way up to the top surface while for regeneratively nucleated PG the cones have apices at all levels.

The second aspect of the microstructure of PG, namely pores, account for approximately 5 percent of the volume as evidenced by the smaller density of PG (2.10 g/c.c) compared to that of ideal graphite (2.25 g/c.c). These pores are closed and therefore are not amenable to the conventional BET or permeability analyses. Since the pores are

approximately 200 Å in size, optical micrographs are unable to detect them. The inherent anisotropy of PG is expected to be reflected in the pore geometry. The first evidence of these submicroscopic pores was provided by Bragg et al. (70) in their study of the orientation dependent SAXS. These authors suggested an interpretation of the SAXS as arising from a dilute monodisperse collection of oblate ellipsoids of revolution with the common minor-axis approximately perpendicular to the deposition plane. The presence of a strong texture in PG gives rise to "double Bragg" diffraction that appears at very small angles (70). This contribution can either be suppressed using suitable wavelengths that do not Bragg reflect from the layer planes or it has to be identified so as not to confuse it with true SAXS.

C. Theory

Hamzeh and Bragg have proposed a theory (71) of SAXS by oriented ellipsoids of revolution. The scattering has been shown to be in the form of Rayleigh scattering by "Guinier spheres" whose radii depend upon the orientation of the ellipsoids relative to the plane of observation.

II. PORE STRUCTURE

A. Introduction

The following work attempts to study the geometry of the pores in PG using SAXS. The SAXS is anisotropic and the theory proposed below has general application for other anisotropic cases such as non-spherical precipitates in two phase systems, spinodal decomposition in magnetic and stress fields where the morphology of the minor phase is deliberately made anisotropic for technological reasons.

B. Theory

In their theory (71) Hamzeh and Bragg made the assumption that the phase difference, δ, between the beam scattered at Z = 0 and Z = Z, (Fig. 17 and Z axis coincident with $\bar{h}_o$) is approximately hZ, where $|h| = 4\pi\sin\theta/\lambda$. This approximation is valid only for γ close to zero. Rothwell had put forward a treatment of SAXS from ellipsoids (72) which does not have this restriction but it leads to the same intensity expression. However, the possibibility of next generation of complicated geometries like semi-ellipsoid, shapes that are composites of two semi-ellipsoids joined with common major axis or skin of ellipsoids have not been considered so far even though these geometries are consistent with the optical micrographs showing "growth cones". The intensity calculations for these shapes are done below referring to Fig. 18.

$\bar{S}_o(\lambda)$ and $\bar{S}(\lambda)$ are the incident and the scattered x-ray beams. The path difference between the beam scattered at $O(Z=0)$ and at $P(Z,r,\alpha)$ is given by

$$\Delta = r\,\mathrm{Cos}\alpha\,\mathrm{Sin}\gamma\,\mathrm{Sin}2\theta + Z\,\mathrm{Cos}\gamma\,\mathrm{Sin}2\theta.$$

For small scattering angles, $\mathrm{Sin}2\theta \sim 2\theta$, $\mathrm{Cos}2\theta \sim 1$. Thus the phase difference

$$\delta = (4\pi\theta/\lambda)\,\mathrm{Cos}\alpha\,\mathrm{Sin}\gamma + (4\pi\theta/\lambda)\,Z\,\mathrm{Cos}\gamma$$
$$= h\,\mathrm{Cos}\alpha\,\mathrm{Sin}\gamma + hZ\,\mathrm{Cos}\gamma.$$

The structure factor of a particle of electron density ρ and volume V is

$$f(h,\gamma) = 1/V \int_0^{2\pi} d\alpha \int_0^a r\,dr\,\exp(ihr\mathrm{Sin}\gamma\mathrm{Cos}\alpha) \int_P^Q \exp(ihZ\,\mathrm{Cos}\gamma)\,dZ.$$

For a particle composed of two halves of volume V1 and V2 respectively,

$$F(h,\gamma) = (\rho V1)f1 + (\rho V2)f2$$

where f1 and f2 are the values of the integral $f(h,\gamma)$ for the two halves. The scattered intensity from N particles

$$I(h,H) = NF^2(h,\gamma).$$

The limits of integration for f1 and f2 are P1, Q1, respectively. Then for the case of

ellipsoid	V1 = V2 = V/2, P1 = P2 = 0, Q1 = Q2 = b	
semi-ellipsoid (Fig. 18a)	f2 = 0, V=V1, P1 = 0, Q1 = b	Case (a)
composite (Fig. 18b)	P1 = 0 = P2, Q1 = b_1, Q2 = b_2	Case (b)
skin of ellipsoid (Fig. 18c)	P1 = 0 = P2, Q1 = b_1, Q2 = $-b_2$	Case (c)

Using $\phi(hH) = 3\,[\,\mathrm{Sin}(hH) - hH\,\mathrm{Cos}(hH)]/\,(hH)^3$,

$$H^2 = a^2\mathrm{Sin}^2\gamma + b^2\cos^2\gamma$$

and

$$k = V2/V1 = b_2/b_1$$

one obtains the intensity

$$I(h,H) = NF^2(h,H) = NF^2(h,\gamma) = N/4[\,\rho V1\phi(hH1) \pm \rho V2\ \phi(hH2)]^2.$$

For the case of

(i) full ellipsoid $H1 = H2 = H$, $V1 = V2 = V$ and the plus sign inside the bracket is to be used.

(ii) semi-ellipsoid (case a) $V2 = 0$,

(iii) composite (case b) plus sign is to be used inside the bracket).

(iv) skin (case c) minus sign is to be used inside the bracket.

In the Guinier region $h \to o$ and the trigonometric terms can be expanded to give

$$I(h,H) \underset{h\to 0}{=} (N/4)(\rho V1)^2\,(1\pm k)^2\ \exp[-1/5h^2\ \{a^2\mathrm{Sin}^2\gamma+(b_1^2\pm kb_2^2)/(1\pm k)\cos^2\gamma\}]. \quad (6)$$

Here $k = +$ for full ellipsoid

$= 0$ for case a

> 0 for case b

< 0 for case c

Thus a plot of lnI vs h^2 should give a straight line with a negative slope from which one gets the Guinier radius

$$H = [a^2 \mathrm{Sin}^2\gamma + \{(b_1^2 \pm k b_2^2)/(1\pm k)\}\mathrm{Cos}^2\gamma]^{1/2}. \qquad (7)$$

In the Porod region on the other hand $h \to \infty$ and $hH\ \mathrm{Cos}(hH) >> \mathrm{Sin}(hH)$. Thus,

$$I(h,H) = (9N/8)(\rho V1)^2 (1/h^4)(H^2 + kH1^2)/H1^2 H2^2 \qquad (8)$$
$$h \to \infty$$

k assuming the values indicated above for each case.

Equation (8), for long and narrow slit collimation (44) becomes

$$I(h,H) = (\text{constant})\ 1/h^3\ [H2^2 \pm kH1^2)/H1^2 H2^2]^2 \qquad (9)$$
$$h \to \infty$$

while the Guinier Eq. (6) remains the same except for a constant factor dependent on the size of the particles.

For k = 1, i.e., full ellipsoid (H1 = H2) and k = 0 i.e., for semi-ellipsoid one has

$$[h^3 I(hH)]^{-1/2} = (\text{constant})[(a^2 - b^2)\ \mathrm{Sin}^2\gamma + b^2].$$

If the value of k is close to unity or to zero the above relation still holds good fairly well. However, if k is substantially different from unity or zero the equation is no longer valid. A plot of the left hand side vs $\mathrm{Sin}^2\gamma$ could therefore decide about the relative value of k. In the case of k being unity or zero or close to these we expect a straight line.

C. Material

The foregoing analysis provides the existing theory and that developed in the present work to characterize the oriented pores in PG. Measurements were made on PG samples provided through the courtesy of M/S Pfizer, Inc. The material received had the deposition surface characterized by the designs on the surface. The sample was about 1" thick. Specimen for measurements were cut as shown, Fig. 17a. The mode of preparation of PG clearly indicates that it is isotropic in the deposition plane, Fig. 17b with the common axis of revolution of the pores perpendicular to it. The specimen were thinned to the optimum thickness for maximum scattering i.e., the reciprocal of the linear absorption coefficient of PG for the wavelength used.

D. Experiment

SAXS was recorded by an AMR 6-220 x-ray low angle scattering goniometer based on a design by Bonse and Hart (74). It consists of two grooved perfect Ge crystals in parallel position with the sample holder placed between them as in Fig. 19. The depth of the groove is approximately 1.5 cms. The walls of the crystal grooves are parallel to the (220) planes of Ge. The x-ray beam is reflected six times between the walls in each Ge crystal. This results in the effective elimination of the tail of the reflection curve (74). The second crystal is rotated about a vertical axis through the center of the sample by means of a large barrel micrometer calibrated in steps of one second of arc θ. It is driven by a motor. The counter is a Philips scintillation detector connected to a scaler, ratemeter, pulse height analyzer and a

teletype output. A rocking curve recording the direct beam showed that one could approach within 5 seconds of arc θ of the direct beam. Calibrated Ni foils are mounted on a rotating disc to reduce the scattered intensity by a known factor so that the counting rates were within the range of linearily of the detector and the absolute value of I_0 determined.

The Porod region of PG was investigated on a GE XRD-3 diffractometer with slit arrangements discussed earlier in connection with SAXS of GC.

To investigate the isotropy of the pores in PG in a plane parallel to the deposition surface, the specimen of type Fig. 17b was rotated (ϕ) about the incident x-ray beam and the intensity was measured at a fixed scattering angle for various values of ϕ covering the four quadrants. For the orientation, Fig. 17c, the specimen was rotated about the incident beam (γ) and the whole intensity distribution was recorded for each value of γ.

E. Results and Discussion

The scattered intensity distribution as a function of γ for two extreme cases is shown in Fig. 20. For scattering vectors smaller than 2×10^{-2} A^{-1} the presence of "double Bragg" diffraction is clearly evident. The region from which the "Guinier radius" was determined had scattering vectors larger than $2 \times 10^{-2} A^{-1}$ to make sure that no misinterpretations arise. The graph of logarithm of intensity against h^2, called "Guinier plot" usually gives a straight line if the Guinier exponential law is obeyed. From the slope of the straight line Guinier radius is determined.

Typical Guinier plots are shown in Fig. 21. The scattering from a specimen of orientation Fig. 17b was found to be independent of the angle of rotation ϕ of the sample about the incident beam. This is shown in Fig. 22. A direct measurment of $\underline{2a}$ was made from the Guinier plots of the data used to obtain Fig. 22 using $\gamma = 90^{o}$ in Eqs. (6) and (7). This gave 2a = 214 Å. From the plots like Fig. 21, values of H was determined as a function of γ using Eq. (7). Since the number of voids is of the order of 6×10^{5}/cc, their average separation exceeds 500 Å, much larger than pore size. Thus for all practical purposes the influence of interparticle interference (44) on Guinier radius may be neglected. Figure 23 shows the observed γ dependence of H along with the calculated least square fit curve using

$\underline{2a}$ = 228Å, 2b = 152Å (ellipsoid and semi-ellipsoid)

$\underline{2a}$ = 228Å, $2(b_1^2 \pm kb_2^2)/(1 \pm k)^{1/2}$ = 152Å with k = 0.9 (composite).

For the skin of ellipsoid model a good fit needed a large value of k which has been unable to explain the behavior of the Porod region discussed below.

In the Porod region the intensity measured with an effectively long and narrow slit geometry has been found to follow $h^3 I$ = constant, the constant differing for each value of γ. This is shown in Fig. 24. One can see that for larger values of h the product indeed becomes constant for each vlaue of γ. These constant values were used to plot $h^3 I^{-1/2}$ against $\sin^2\gamma$ shown in Fig. 25. The curve obtained is a straight line. This is exactly what one expects for a full as well as semi-ellipsoid. However, if k is close to unity (composite) or to zero (skin)

a straight line dependence would also result. Since the skin model needed a relatively large value of k in the Guinier region it is rejected. The full ellipsoid, the semi-ellipsoid and the composite that give exactly the same agreement in both the Guinier and the Porod region yield

$\underline{2a}$ = 228Å, $\underline{2b}$ = 152Å (full and semi-ellipsoid)

$\underline{2a}$ = 228Å, $\underline{b_1}$ = 80Å, $\underline{b_2}$ = 72Å, k = 0.9 (composite).

Since it is well known that diffraction pattern of an asymmetric object will have a center of symmetry (76), it is not possible to distinguish by x-ray scattering experiments alone between a full ellipsoid, semi-ellipsoid and a composite model. However, it has been found that the interlayer separation in PG, as determined by XRD, increases as one goes from the heated substrate further up. In other words this means that the closer a region is to the substrate the more ordered it will be. This indicates the unlikeliness of the two halves of the ellipsoidal pores to be equal, or in other words it speaks in favor of the model of Fig. 18(b), $b_1 \neq b_2$.

A striking demonstration of the asymmetry of SAXS from PG is shown in Fig. 26 and Fig. 27. The data are computer printouts of two dimensional SAXS data using position sensitive detectors. The connected curves are isointensity contours. The data show clearly that in orientation, Fig. 17(b), the scattering is approximately isotropic, i.e., of circular cross-section on the average, and the isointensity contours are

approximately elliptical for Fig. 18(a-c).

The work on the pore structure of PG has been presented in two conferences (77, 78) and has been accepted for publication in J. Appl. Phys., Preprint (79).

REFERENCES

1. T. Noda, M. Inagaki and S. Yamada, J. Non-Crystalline Solids 1, 285 (1969).
2. G. M. Jenkins and K. Kawamura, Polymeric Carbons, Cambridge University Press, Cambridge (1976).
3. L. Pauling, The Nature of Chemical Bond, 3rd Edition, Cornell University Press, Ithaca, N. Y. (1960).
4. L. Pauling, Proc. U. S. Nat. Acad. Sci., 56, 1646 (1966).
5. S. Ergun, Nature Phys. Sci., 241, 65 (1973).
6. J. Donohue, Nature, 255, 172 (1975).
7. P. Trucano and R. Chen, Nature, 258, 136 (1975).
8. R. Chen and P. Trucano, Acta. Cryst., A33, 823 (1977).
9. E. Fitzer, W. Schaefer and S. Yamada, Carbon, 7, 643 (1969).
10. R. Saxena, The Structure and Electrical Properties of Glassy Carbon, Ph.D. Thesis, Materials Science, University of California, Berkeley (1976).
11. S. Ergun and V. H. Tiensuu, Acta. Cryst., 12, 1050 (1959).
12. T. Noda and M. Inagaki, Bull. Chem. Soc. Japan, 37, 1534 (1964).
13. K. Furukawa, J., Cryst. Japan, 6, 101 (1964).
14. J. Kakinoki, Acta. Cryst., 18, 578 (1965).
15. M. Nakamizo and R. Kammereck, Proceedings of the 11th Biennial Conference on Carbon, Gatlinburg, Tennessee (1973).
16. M. I. Nathan et al., I.B.M. Research RC 4674 (1974).
17. R. R. Saxena and R. H. Bragg, Carbon, 12, 210 (1974).

18. S. Ergun and R. R. Schehl, Carbon, 11, 127 (1973).

19. F. Rousseaux and D. Tchubar, Carbon, 15, 55 (1977).

20. Ibid, 15, 63 (1977).

21. Par A. Oberlin and F. Rousseaux, J. Appl. Cryst., 1, 218 (1968).

22. A. G. Whittaker and B. Tooper, J. Amer. Ceram. Soc., 57, 443 (1974).

23. J. L. Kaae, Carbon, 13, 246 (1974).

24. R. Saxena and R. H. Bragg, LBL Report #5799 (1977).

25. D. B. Fischbach, Chem. and Phys. of Carbon (Ed. P. L. Walker, Jr.) Marcel Dekker, Inc., New York, 7, 1 (1971).

26. A. Pacault, ibid, 7, 107 (1971).

27. S. K. Das and E. E. Hucke, Carbon, 13, 33 (1975).

28. T. Yamaguchi, Carbon, 1, 47 (1973).

29. K. Kawamura and T. Tsuzuku, Carbon, 12, 354 (1974).

30. K. Kamiya and K. Suzuki, Carbon, 13, 317 (1975).

31. T. Noda and H. Kato, Carbon, 3, 289 (1965).

32. W. C. Chard, R. D. Reiswig, L. S. Levinson and T. D. Baker, Carbon 6, 950 (1968).

33. J. M. Cowley, Acta Cryst., 12, 367 (1959).

34. R. Gronsky, Analysis of Grain Boundary Reactions in Al-Zn Alloys Utilizing Lattic Imating Electron Microscopy, Ph.D. thesis, University of California, Berkeley (1976).

35. G. M. Jenkins, K. Kawamura and L. L. Ban, Proc. Roy. Soc. London. Ser. A., 237, 501 (1972).

36. L. L. Ban and W. M. Hess, Proceedings of the 10th Biennial Conference on Carbon, Lehigh University, Bethlehem, Pa. (1971).

37. V. A. Philips, Metallography, 6, 361 (1973).

38. S. Bose, U. Dahmen, R. H. Bragg and G. Thomas, LBL Report-6227 (1977).

39. S. Bose and R. H. Bragg, LBL Report-6649 (1978).

40. D. B. Fischbach and M. E. Rorabaugh, Deutsche Keramische Gesellschaft, Carbon'76, (1976), p.185.

41. W. S. Rothwell, J. Appl. Phys., 39, 1840 (1968).

42. R. Peret and W. Ruland, J. Appl. Cryst., 5, 183 (1972).

43. G. Porod, Small Angle X-ray Scattering, (Ed. H. Brumberger), Gordon and Beach, New York (1967).

44. A. Guinier and G. Fournet, Small Angle Scattering of X-rays, John Wiley and Sons, Inc., London (1955).

45. Par D. Tchoubar and J. Mering, J. Appl. Cryst., 2, 128 (1969).

46. S. Bose and R. H. Bragg, LBL Report-6656 (1977).

47. R. Hoseman and S. N, Bagchi, Direct Analysis of Diffraction by Matter, North-Holland Publishing Co., (1962).

48. W. Ruland, J. Appl. Cryst., 4, 70 (1971).

49. V. Gerold, Small Angle X-ray Scattering (Ed. H. Brumberger) Gordon and Beach, New York (1967).

50. R. M. Meyer and P. A. Thrower, Proceedings of the 10th Biennial Conference on Carbon, Lehigh University, Bethlehem, Pa. (1971).

51. P. A. Thrower, Carbon, 6, 687 (1968).

52. E. S. Golovina, V. S. Chaplygina and L. L. Kotova, Carbon, 8, 125 (1970).

53. M. A. Kanter, Phys. Review, 107, 655 (1957).

54. R. S. Sach and W. J. Williams, Carbon, 12, 425 (1974).

55. JANAF tables.

56. R. J. Good, L. S. Girifalco and G. J. Kraus, J. Phys. Chem., 62, 1418 (1958).

57. H. E. Martens and J. D. Jaffe, J. Appl. Phys., 31, 1122 (1960).

58. O. J. Guentert, J. Chem. Phys., 37, 884 (1962).

59. O. J. Guentert and S. Cvikevich, Proc. of 5th Carbon Conference (Pergamon Press, Inc., New York 1962) Vol. 1, p. 473.

60. O. J. Guentert and C. A. Klein, Appl. Phys. Letters, 2, 125 (1963).

61. J. Pappis, S. Cvikevich, L. Hagen and N. Viola in High Temperature Materials II, Eds. G. M. Ault, W. F. Barclay and H. P. Munger (Interscience Publishers, Inc., New York, 1963), p. 419.

62. O. J. Guentert and S. Cvikevich, Carbon 1, 309 (1964).

63. R. H. Bragg and C. M. Packer, Nature 195, 1080 (1962).

64. R. H. Bragg, D. D. Crooks, R. W. Fenn, Jr., and M. L. Hammond, Carbon, 1, 171 (1964).

65. T. Noda, M. Inagaki and H. Kato, Bull. Chem. Soc., Japan, 35, 1471 (1962).

66. E. R. Stover in High Temperature Materials II, Eds. G. M. Ault, W. F. Barclay and H. P. Munger (Interscience Publishers, Inc., New York, (1963), p. 437.

67. C. David, P. Sublet, A. Auriol and J. Rappeneau, Carbon, 1, 139 (1964).

68. W. V. Kotlensky and H. E. Martens, J. Am. Ceram. Soc., 48, 135 (1964).

69. D. B. Fischbach, J. Appl. Phys. 37, 2202 (1966).

70. R. H. Bragg, M. L. Hammond, J. C. Robinson and Paul L. Anderson, Nature, 200, 555 (1963).

71. F. M. Hamzeh and R. H. Bragg, J. Appl. Phys. 45, 3189 (1974).

72. W. S. Rothwell, J. Math. Phys. 4, 1334 (1963).

73. A. Guinier, X-ray Diffraction, W. H. Freeman and Co., San Francisco and London (1963), p. 342.

74. V. Bonse and M. Hart, Appl. Phys. Letters, 7, 288 (1965).

75. M. M. Biswal and R. H. Bragg, Optics of Bonse-Hart Apparatus, LBL Report-805 (1972).

76. G. Harburn, C. A. Taylor and T. R. Welberry, Atlas of Optical Transforms, Cornell University Press, Ithaca, New York (1975) Plates 2 and 31.

77. S. Bose and R. H. Bragg, Deutsche Keramische Gesellschaft, Carbon '76, (1976) p. 201.

78. S. Bose and R. H. Bragg, Fourth International Conference on Small Angle Scattering of X-rays and Neutrons, Gatlinberg, Tennessee (1977) p. 32.

79. S. Bose and R. H. Bragg, LBL Report-6655 (1977).

80. O. L. Blakslee, D. G. Proctor, E. J. Seldin, G. B. Spence and T. Weng, J. Appl. Phys., 41, 3373 (1970).

81. B. P. Richards and E. A. Kellett, U. K. Atomic Energy Authority Report A.E.R.E./EMR PR 1326, 1967.

82. E. A. Kellett and B. P. Richards, J. Nuclear Mater 12, 184 (1964).

FIGURE CAPTIONS

Fig. 1. Selected area electron diffraction pattern of GC.

Fig. 2. Lattice image of GC showing (00.1) planes of spacing 3.4Å. Inset shows the "Jenkin's Model".

Fig. 3. Bending of the layer planes.

Fig. 4. XRD pattern of GC before correction.

Fig. 5. Corrected XRD line profile of GC.

Fig. 6. Kinetics of density change in GC.

Fig. 7. Density of GC as a function of heat treatment temperature.

Fig. 8. Effect of sharp edges and corners of particles on the SAXS profile.

Fig. 9. Typical Porod plot of SAXS from GC.

Fig. 10. Typical Guinier plot of SAXS from GC.

Fig. 11. Plot to determine the Porod invariant in SAXS from GC.

Fig. 12. Radius of gyration kinetics of pores in GC.

Fig. 13. Specific surface area kinetics of pores in GC.

Fig. 14. Specific surface area of pores in GC follows a first order rate law with k as rate constant.

Fig. 15. Activation energy of pore evolution in GC.

Fig. 16. Pore model in GC.

Fig. 17. Geometry of voids

(a) Block of PG
(b) Voids project as circles
(c) Voids project as ellipses
(d) Scattering at voids

Fig. 18. (a) SAXS from a full ellipsoid
(b) Composite ellipsoids
(c) Skin of ellipsoids

Fig. 19. SAXS set up.

Fig. 20. Typical Porod plots for oriented PG.

Fig. 21. Typical Guinier plots for oriented PG.

Fig. 22. Isotropic scattering from a PG specimen cut parallel to the deposition surface.

Fig. 23. Dependence of Guinier radius on orientation.

Fig. 24. Verification of Porod's Law at large values of h.

Fig. 25. Dependence of Porod constant on $Sin^2\gamma$.

Fig. 26. Circular symmetry of scattering from a PG specimen cut parallel to the deposition surface.

Fig. 27. Elliptical symmetry of scattering from a PG specimen cut normal to the deposition surface.

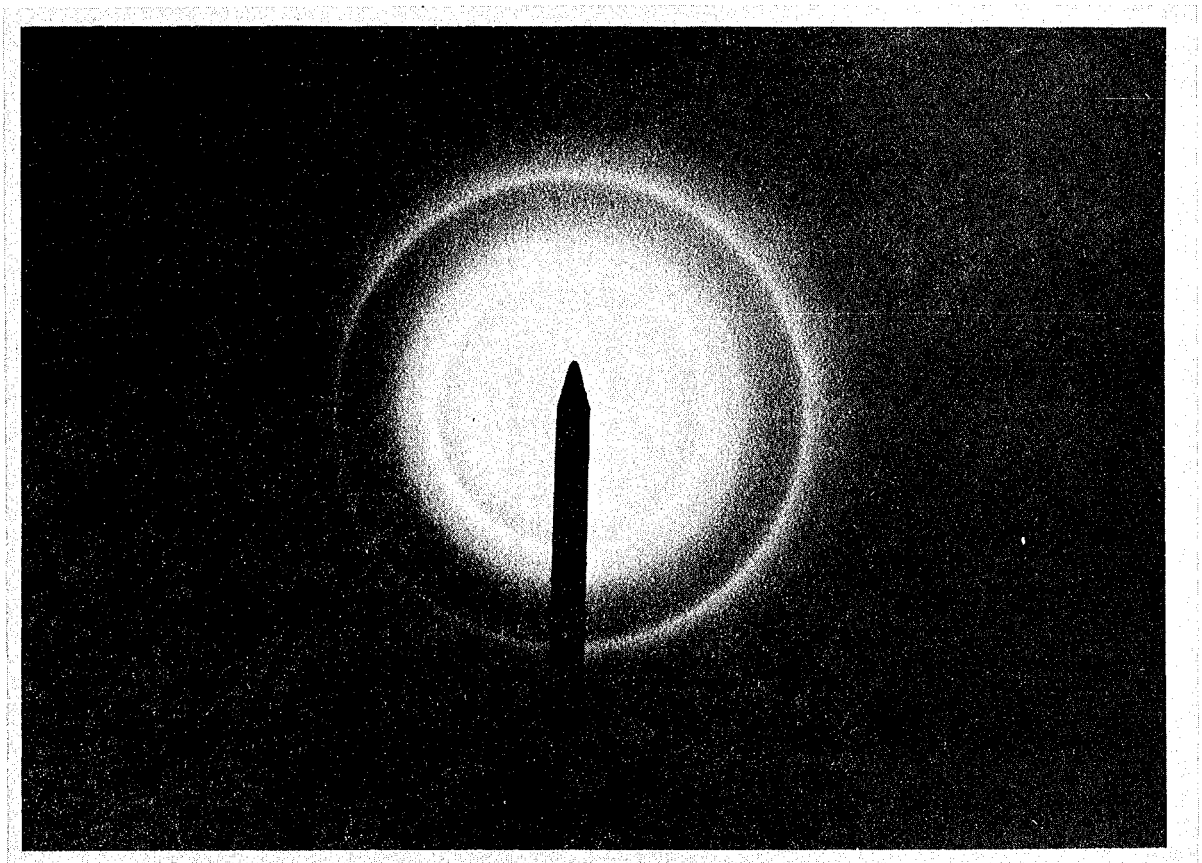

XBB 781-507

Figure 1

XBB 778-7454

Figure 2

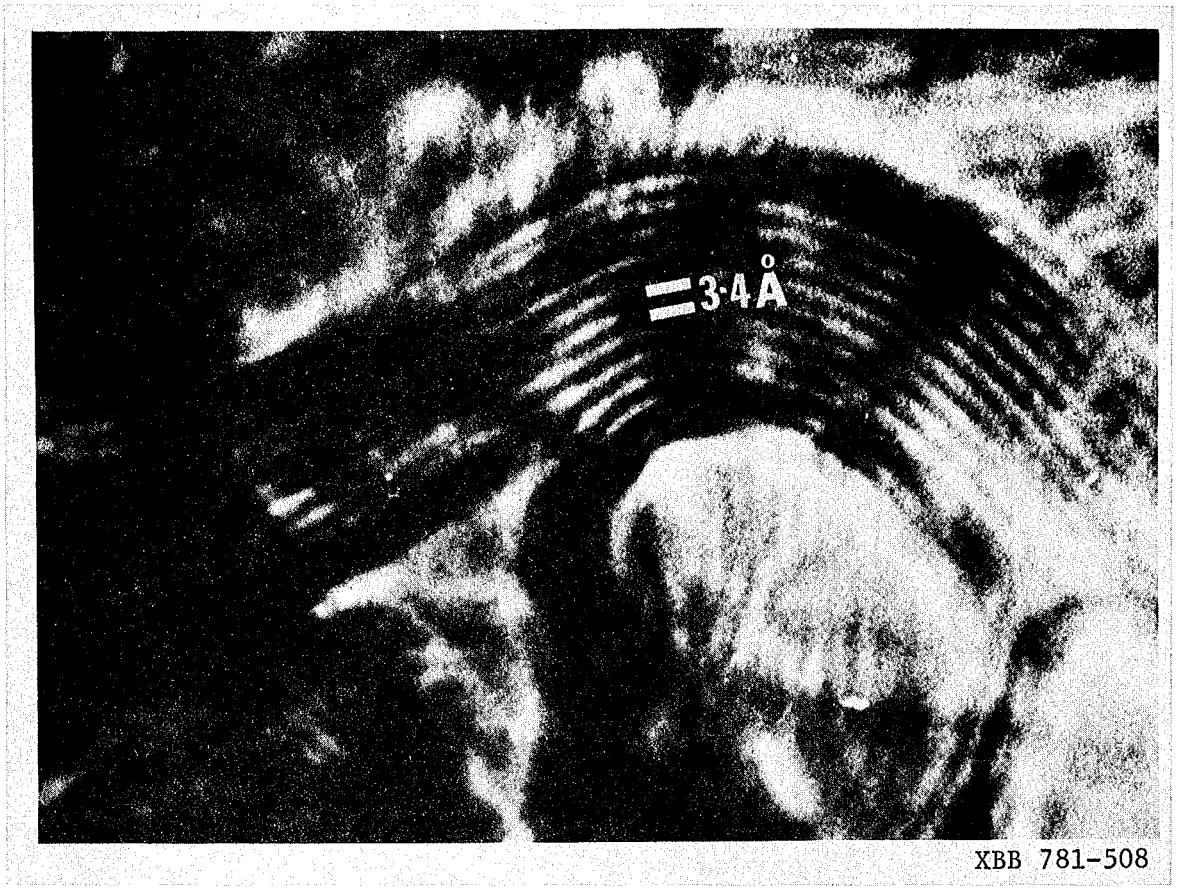

Figure 3

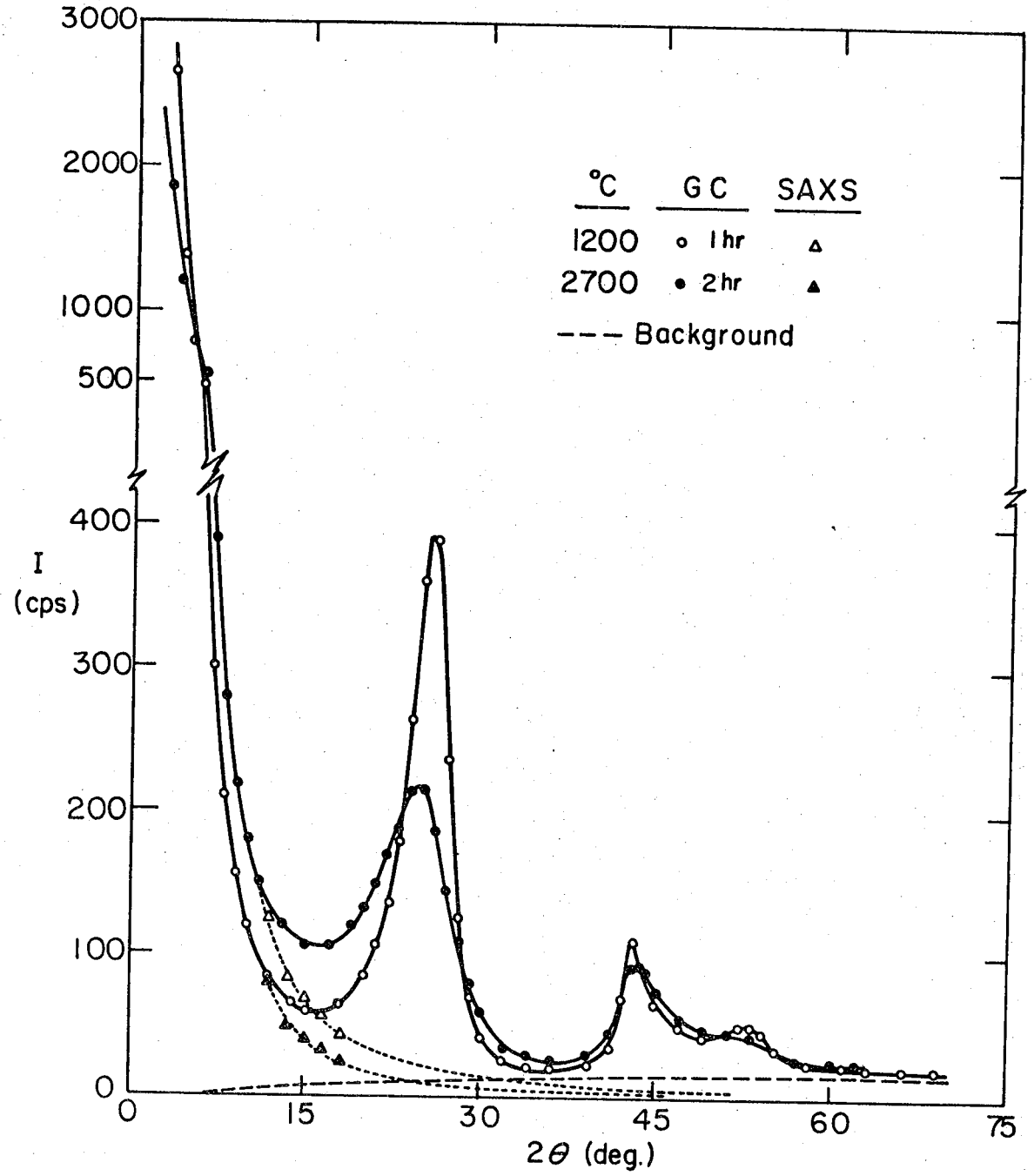
3000
2000
1000
500
400
300
200
100
0
I
(cps)
°C GC SAXS
1200 ○ 1hr △
2700 ● 2hr ▲
--- Background
0
15
30
45
60
75
2θ (deg.)
XBL 7711-6350

Figure 4

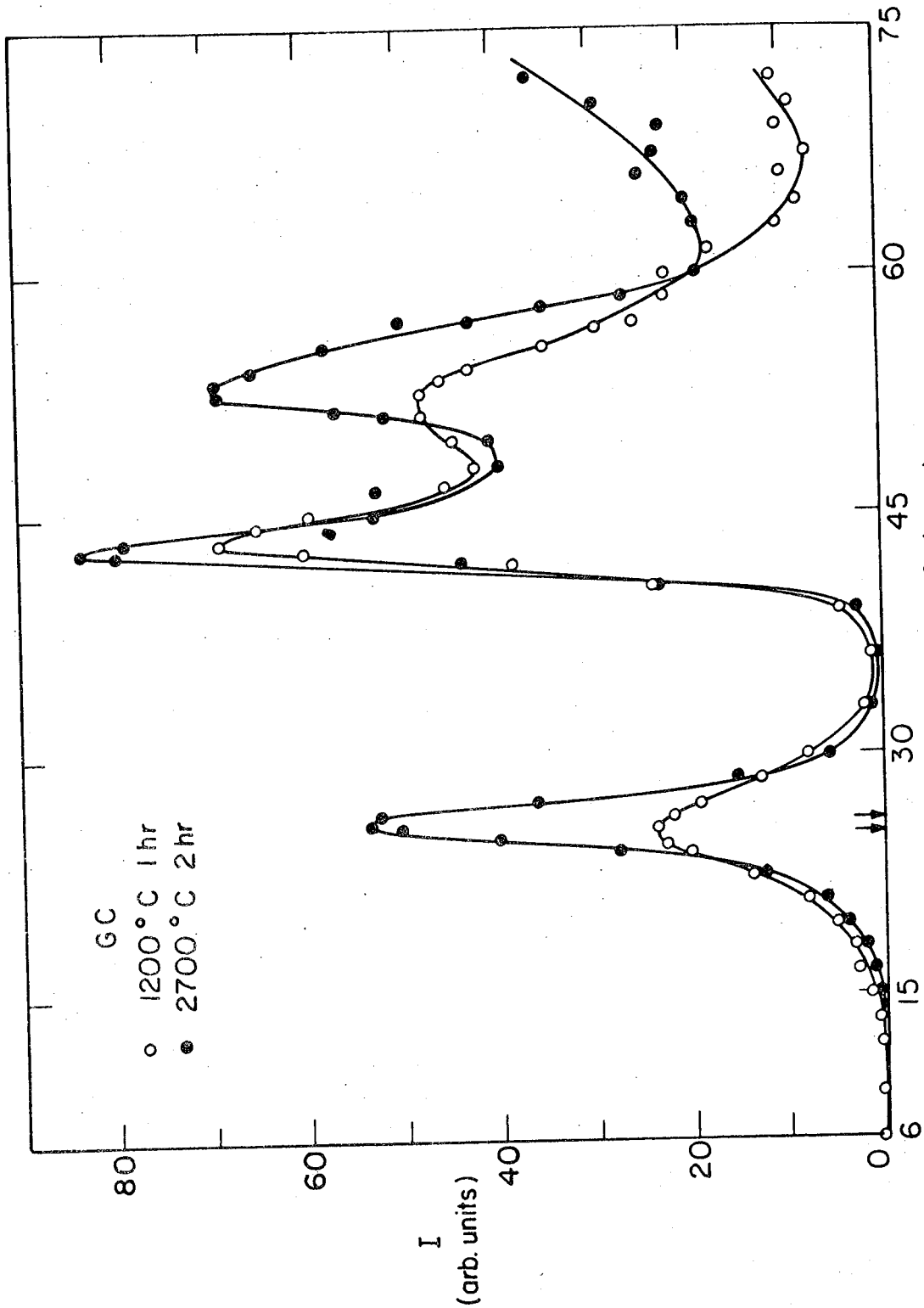

XBL 7711-6355

Figure 5

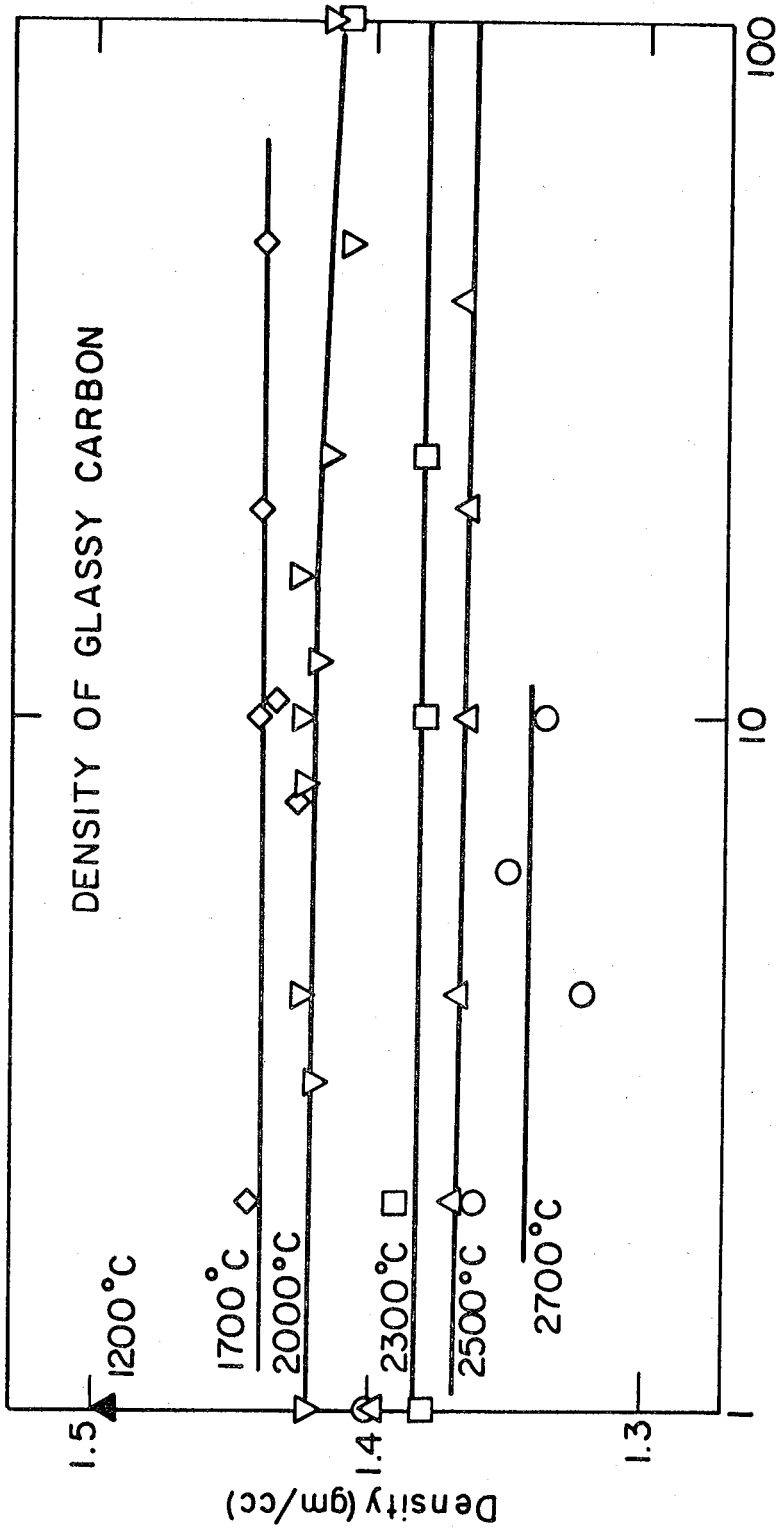
DENSITY OF GLASSY CARBON
1200°C
1700°C
2000°C
2300°C
2500°C
2700°C
1.5
1.4
1.3
Density (gm/cc)
10
100
HTt (Hours)
XBL 776-5645

Figure 6

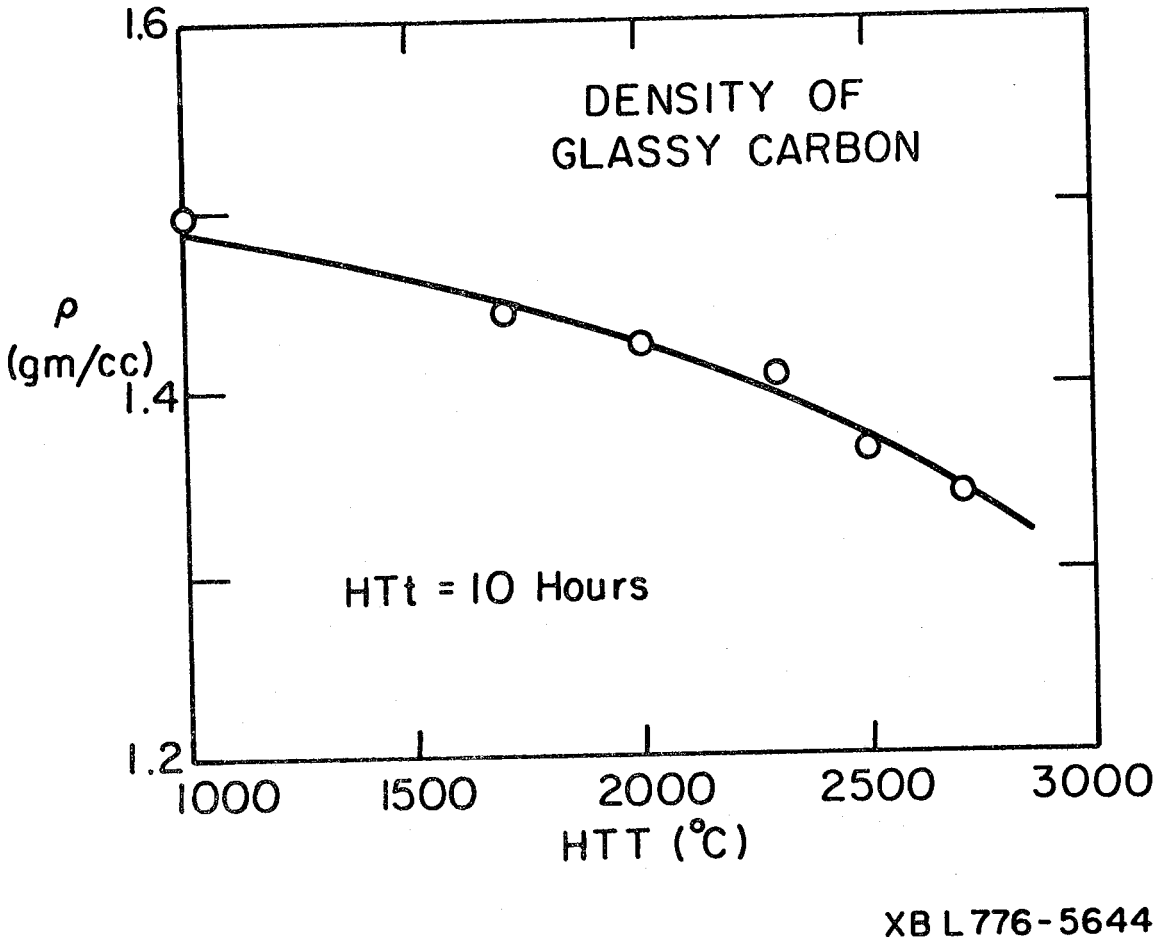
DENSITY OF
GLASSY CARBON
ρ
(gm/cc)
1.6
1.4
1.2
HTt = 10 Hours
1000
1500
2000
2500
3000
HTT (°C)
XBL776-5644

Figure 7

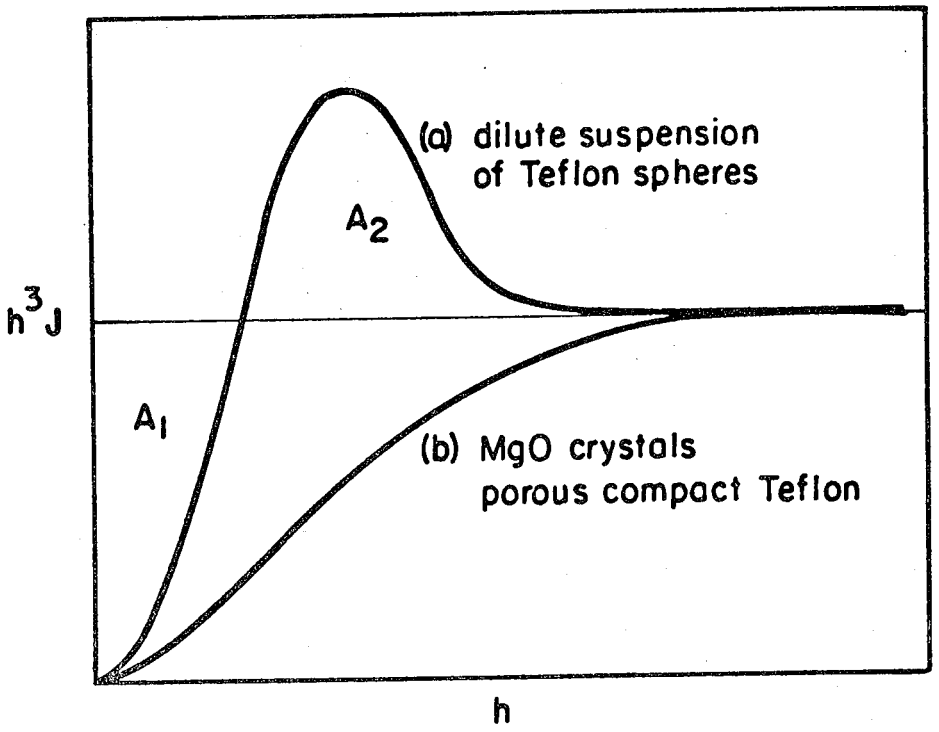

XBL 783-4701

Figure 8

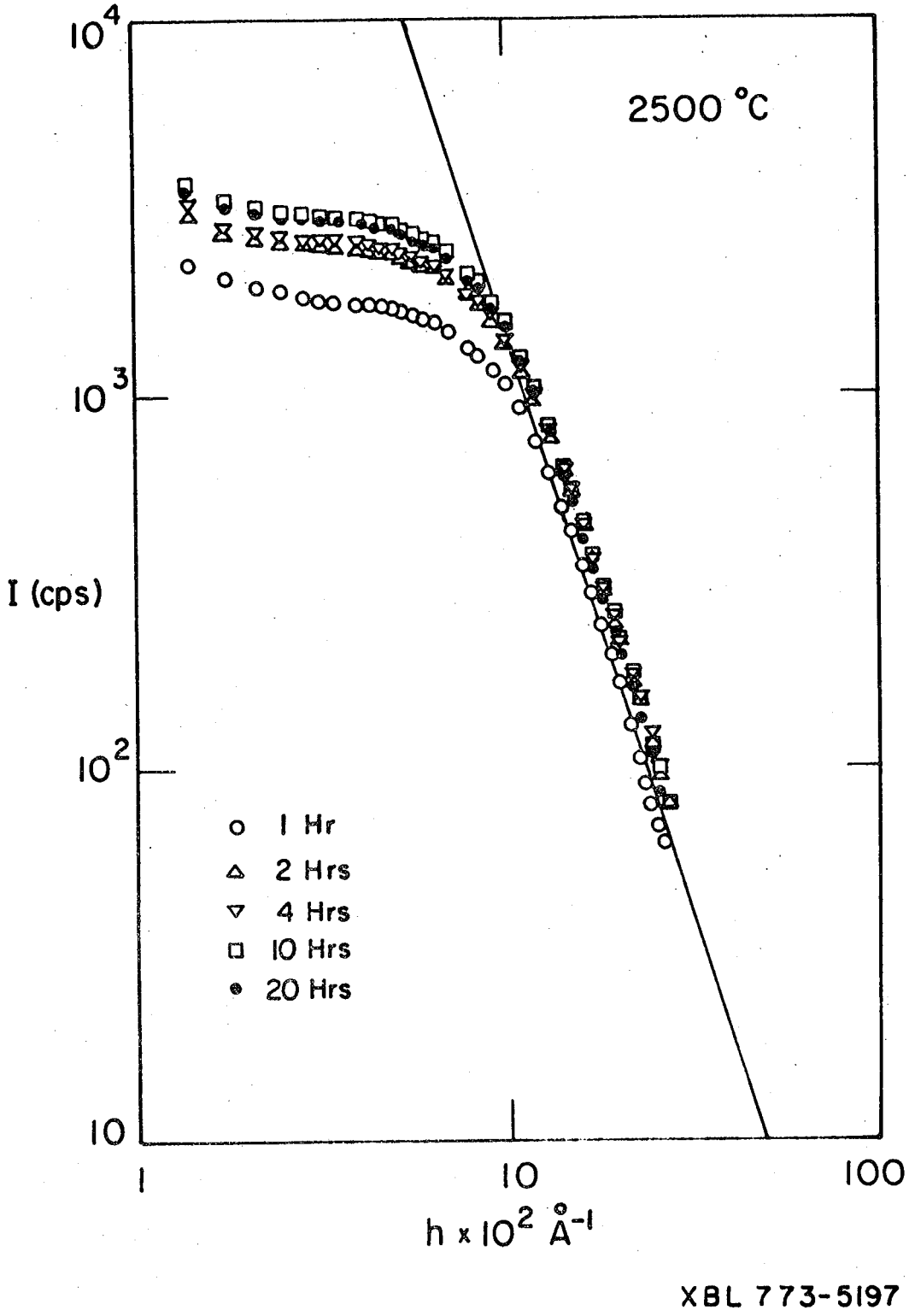
2500 °C
I (cps)
10^4
10^3
10^2
10
1
10
100
h x 10^2 Å^{-1}
1 Hr
2 Hrs
4 Hrs
10 Hrs
20 Hrs
XBL 773-5197

Figure 9

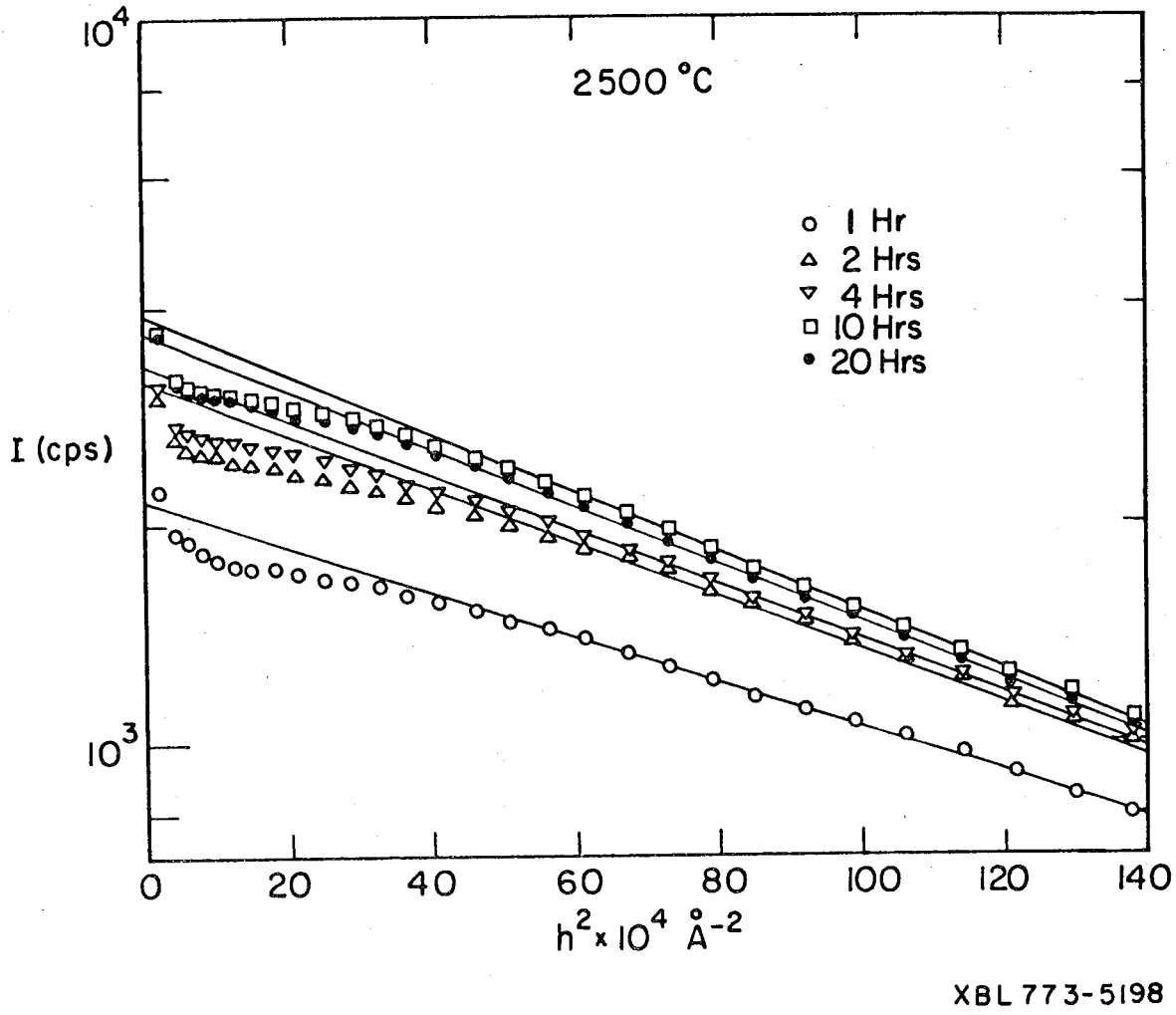
2500 °C
1 Hr
2 Hrs
4 Hrs
10 Hrs
20 Hrs
I (cps)
10^4
10^3
0
20
40
60
80
100
120
140
$h^2 \times 10^4$ Å^{-2}
XBL 773-5198

Figure 10

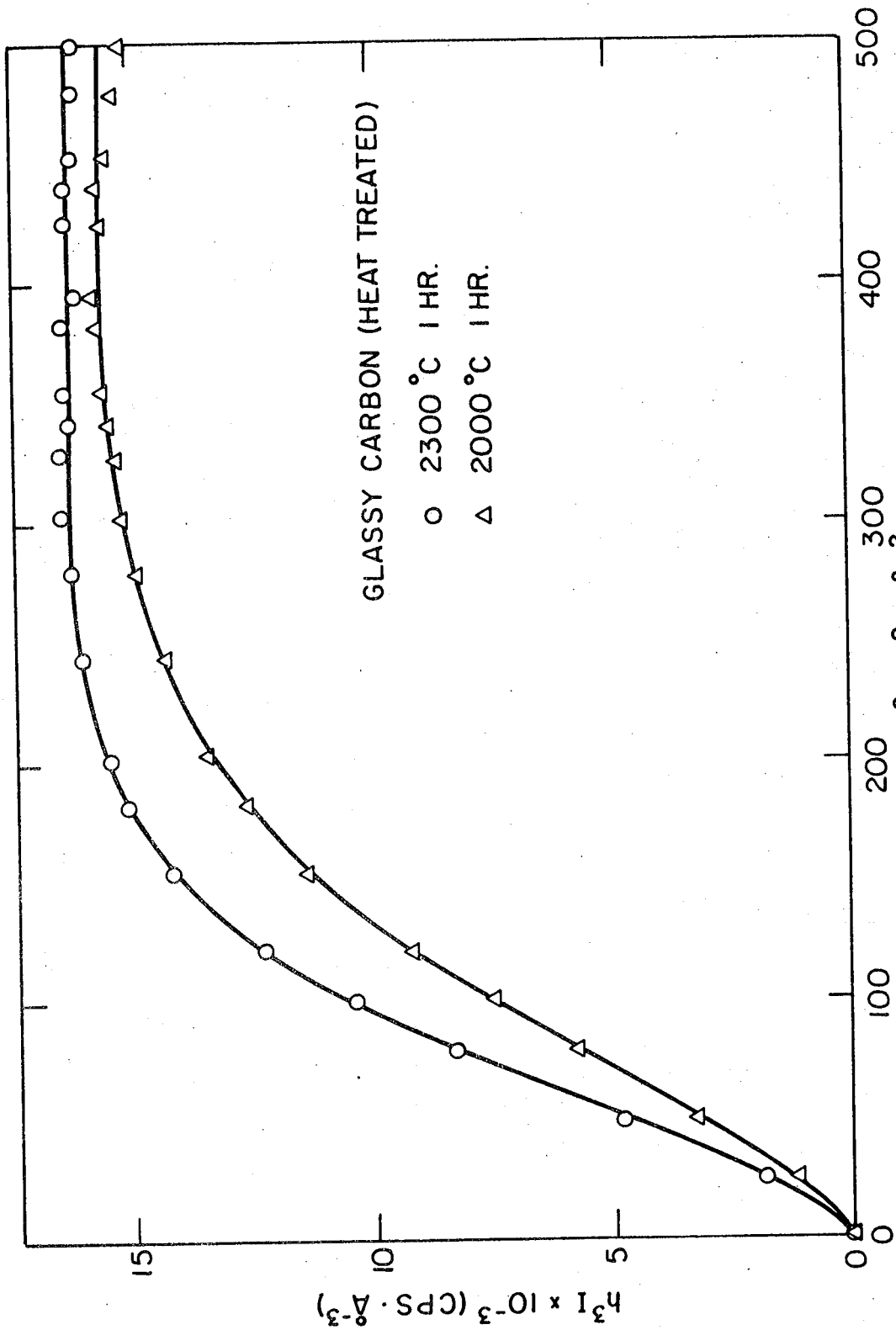

XBL 781-4529

Figure 11

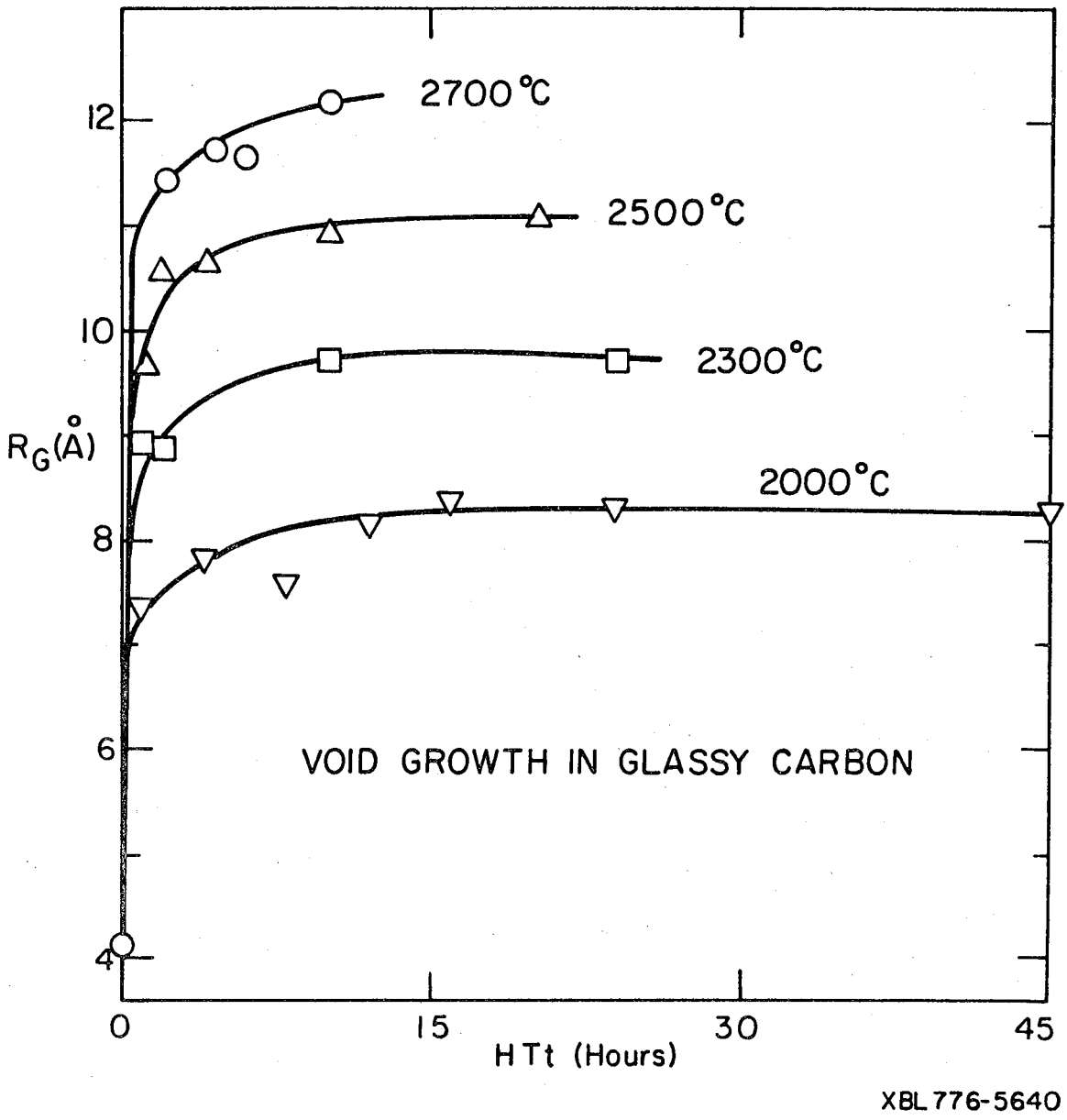
2700°C
2500°C
2300°C
2000°C
VOID GROWTH IN GLASSY CARBON
R_G(Å)
12
10
8
6
4
0
15
30
45
H Tt (Hours)
XBL 776-5640

Figure 12

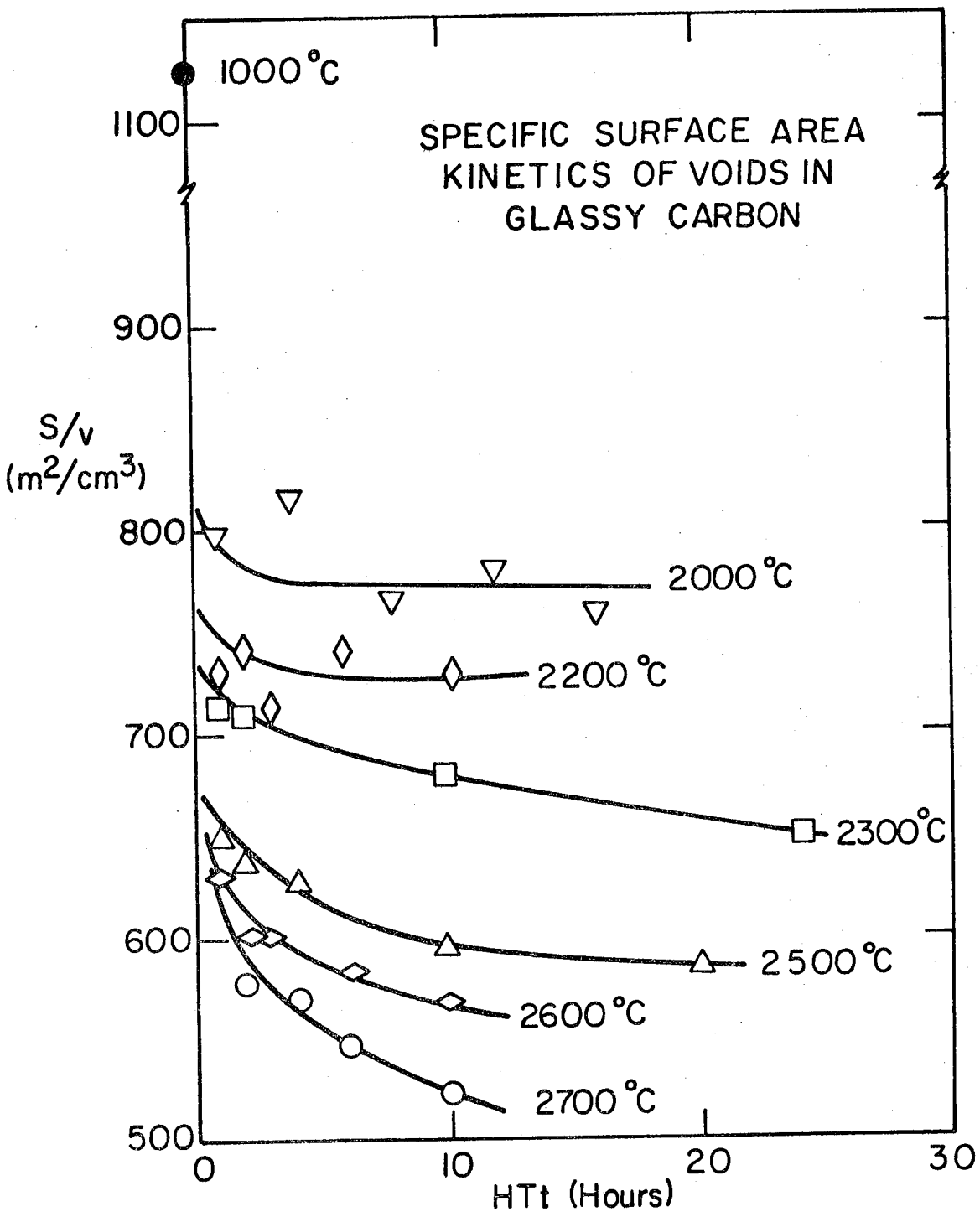

Figure 13 XBL776-5641A

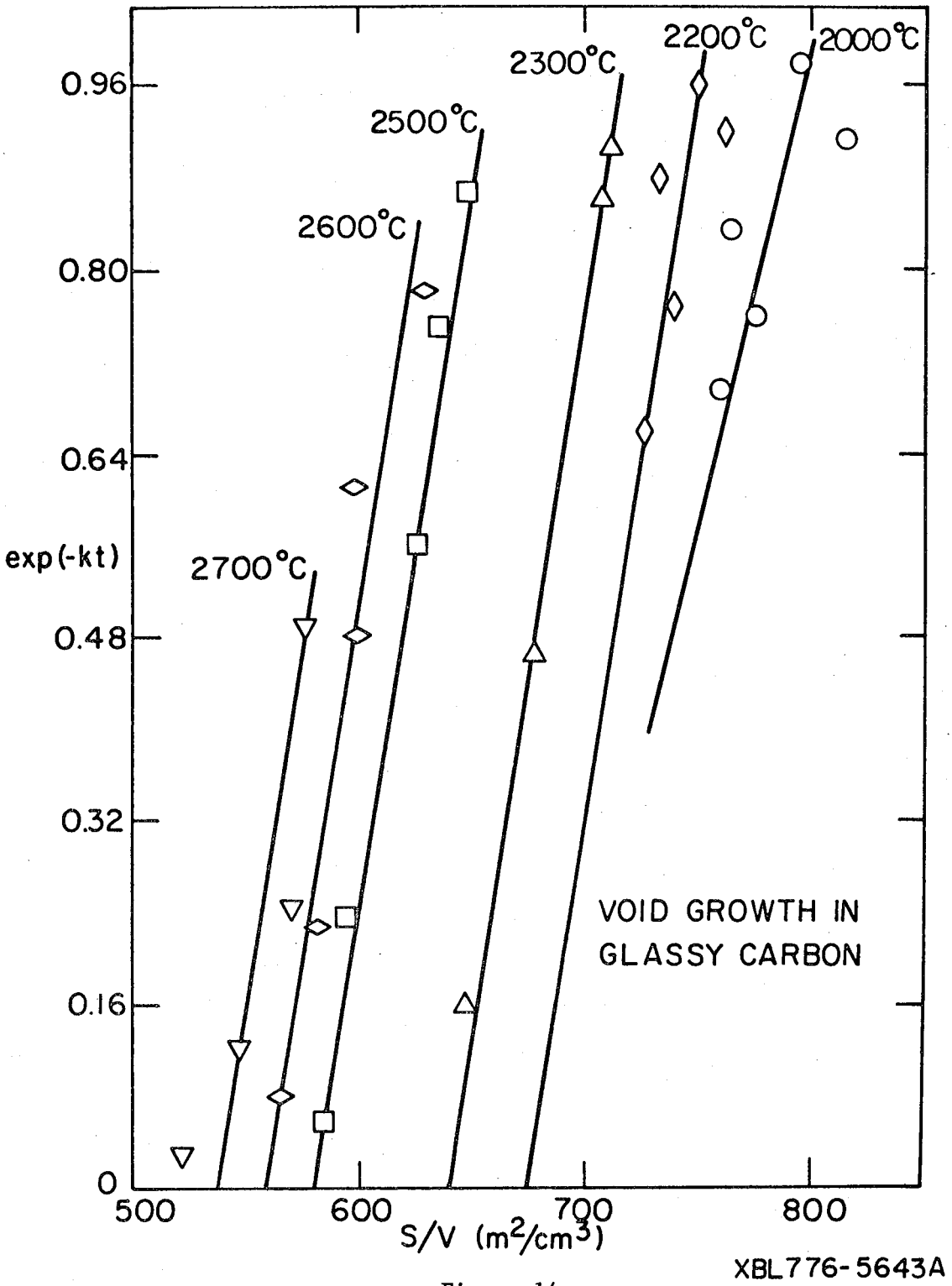
2000°C
2200°C
2300°C
2500°C
2600°C
2700°C
0.96
0.80
0.64
0.48
0.32
0.16
0
exp(-kt)
500
600
700
800
S/V (m²/cm³)
VOID GROWTH IN
GLASSY CARBON
XBL776-5643A

Figure 14

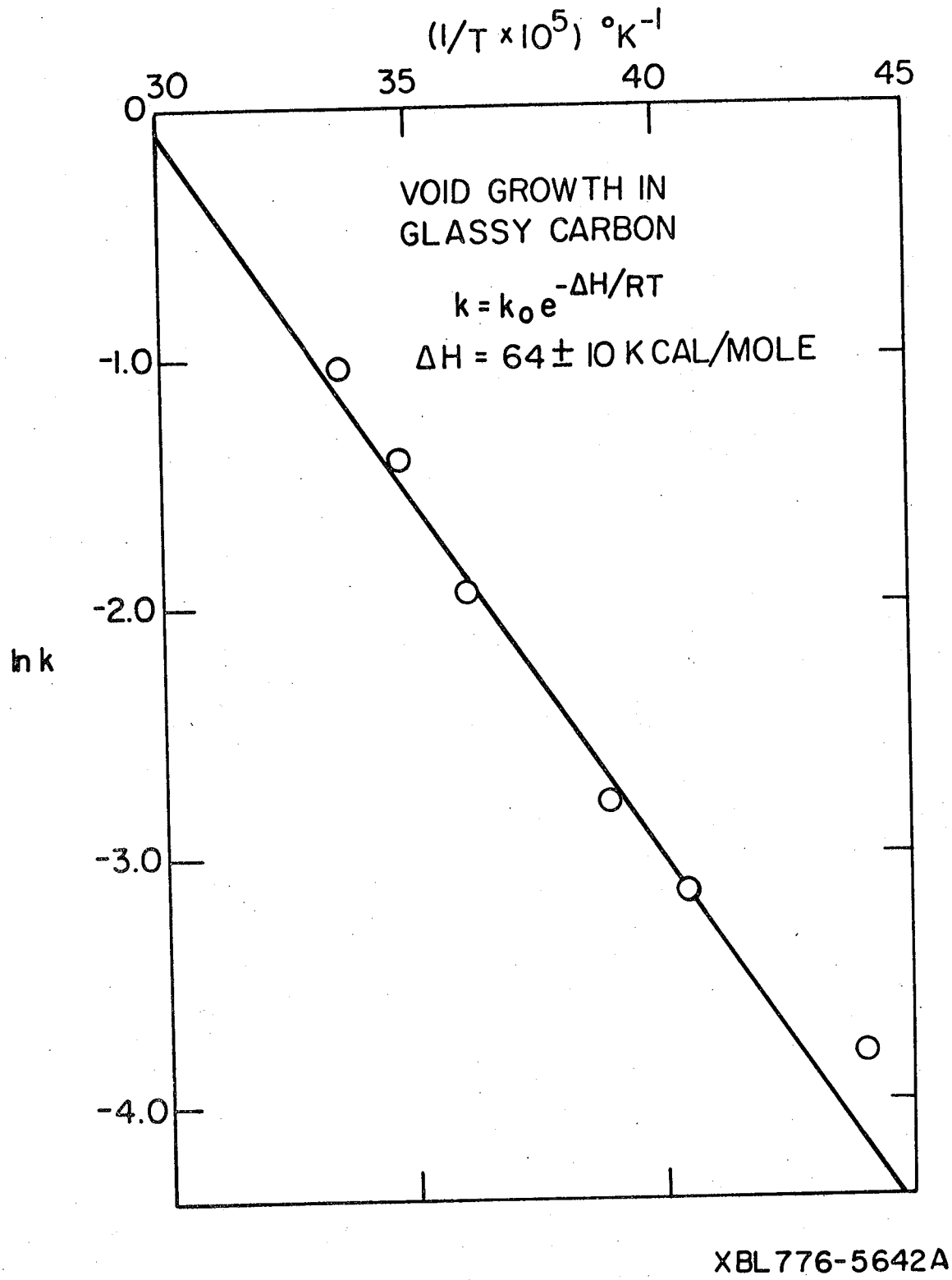
(1/T x 10^5) °K^-1
30
35
40
45
VOID GROWTH IN
GLASSY CARBON
k = k0 e^-ΔH/RT
ΔH = 64 ± 10 KCAL/MOLE
-1.0
-2.0
-3.0
-4.0
ln k
XBL776-5642A

Figure 15

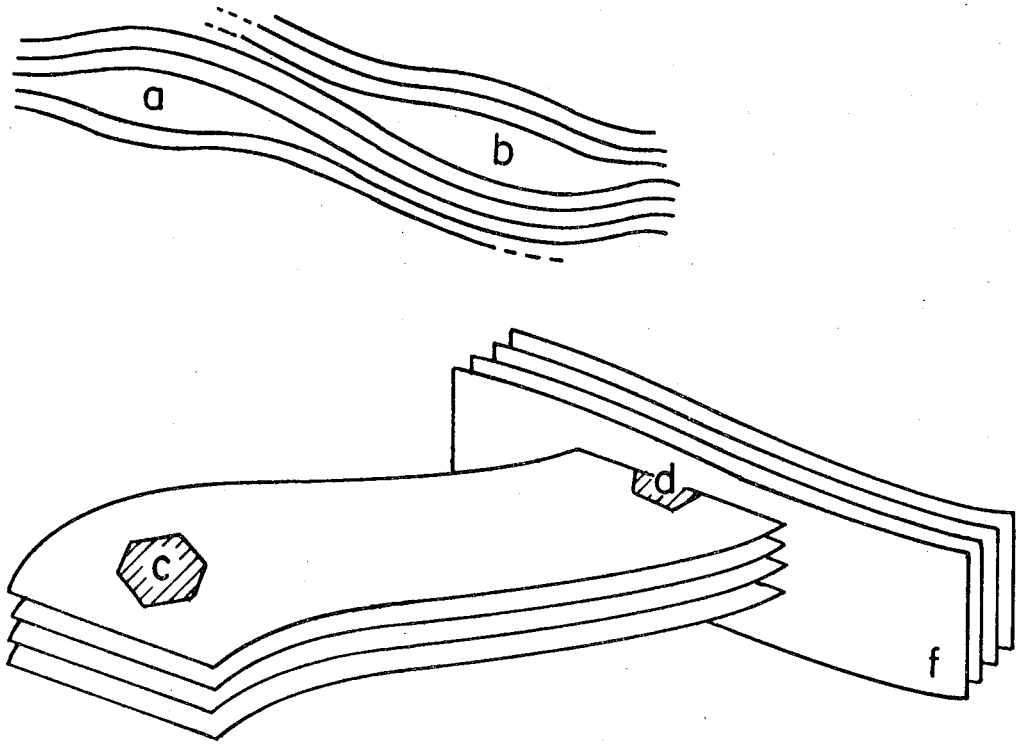

XBL 783-4760

Figure 16

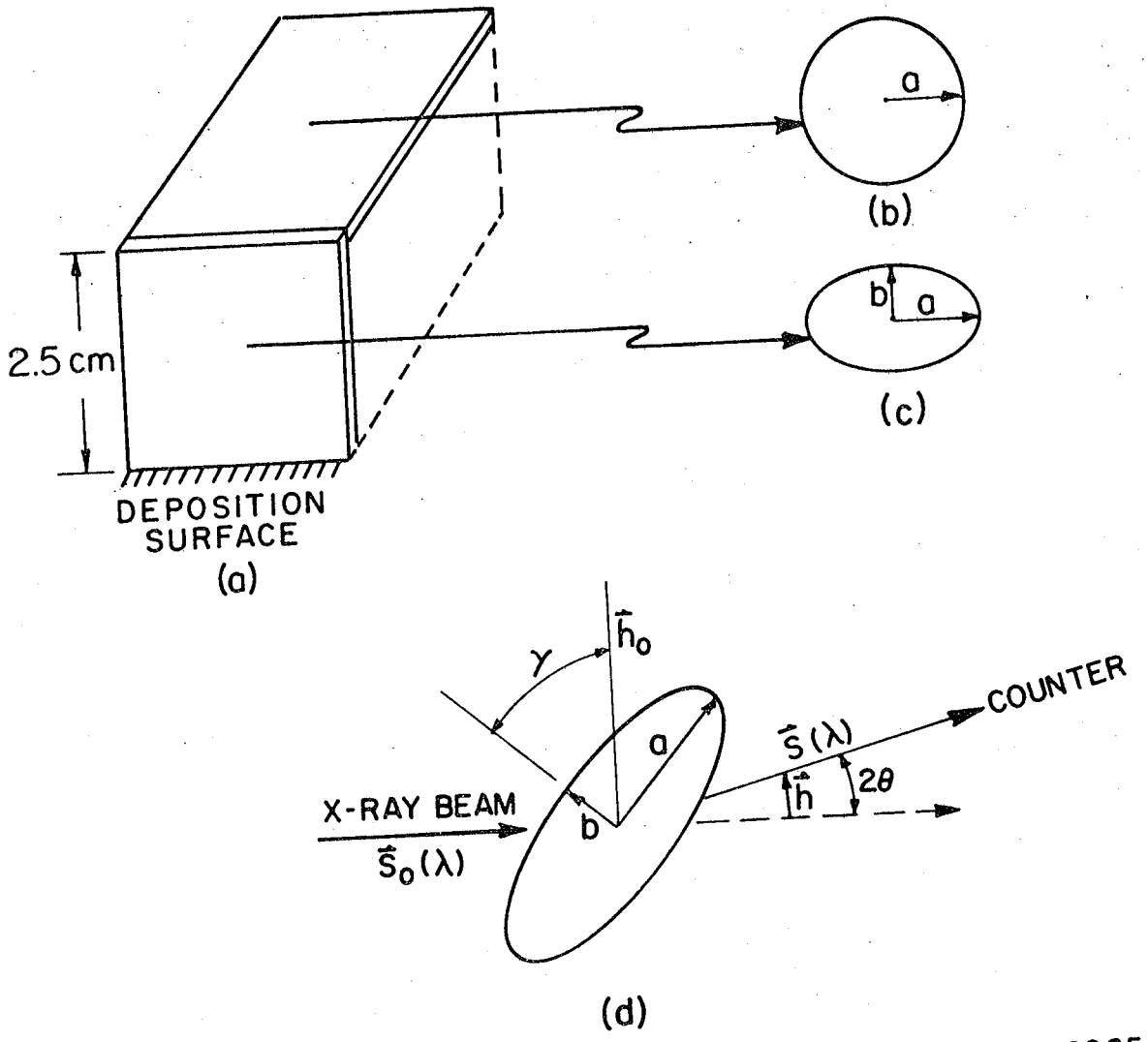
a
(b)
b
a
(c)
2.5 cm
DEPOSITION
SURFACE
(a)
$\vec{h}_o$
γ
a
$\vec{S}(\lambda)$
COUNTER
X-RAY BEAM
$\vec{S}_o(\lambda)$
b
$\vec{h}$
2θ
(d)
XBL 761-6285

Figure 17

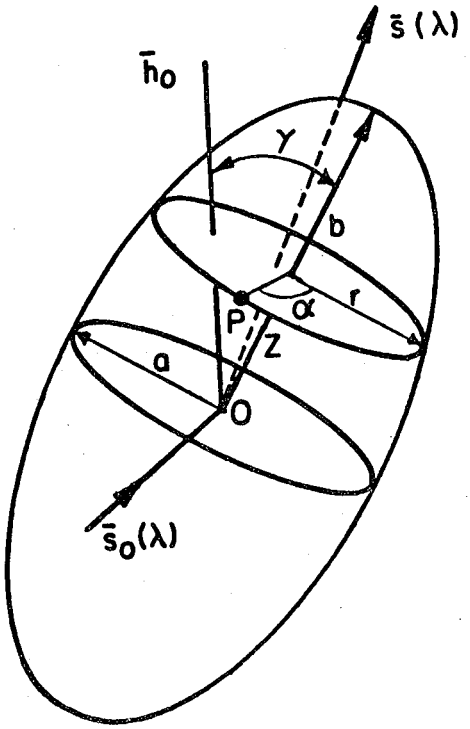

(a)

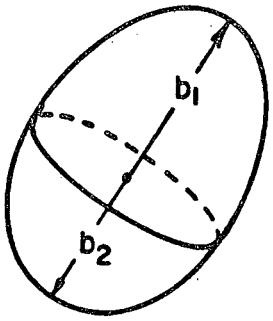

(b)

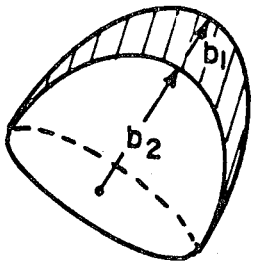

(c)

XBL783-4676

Figure 18

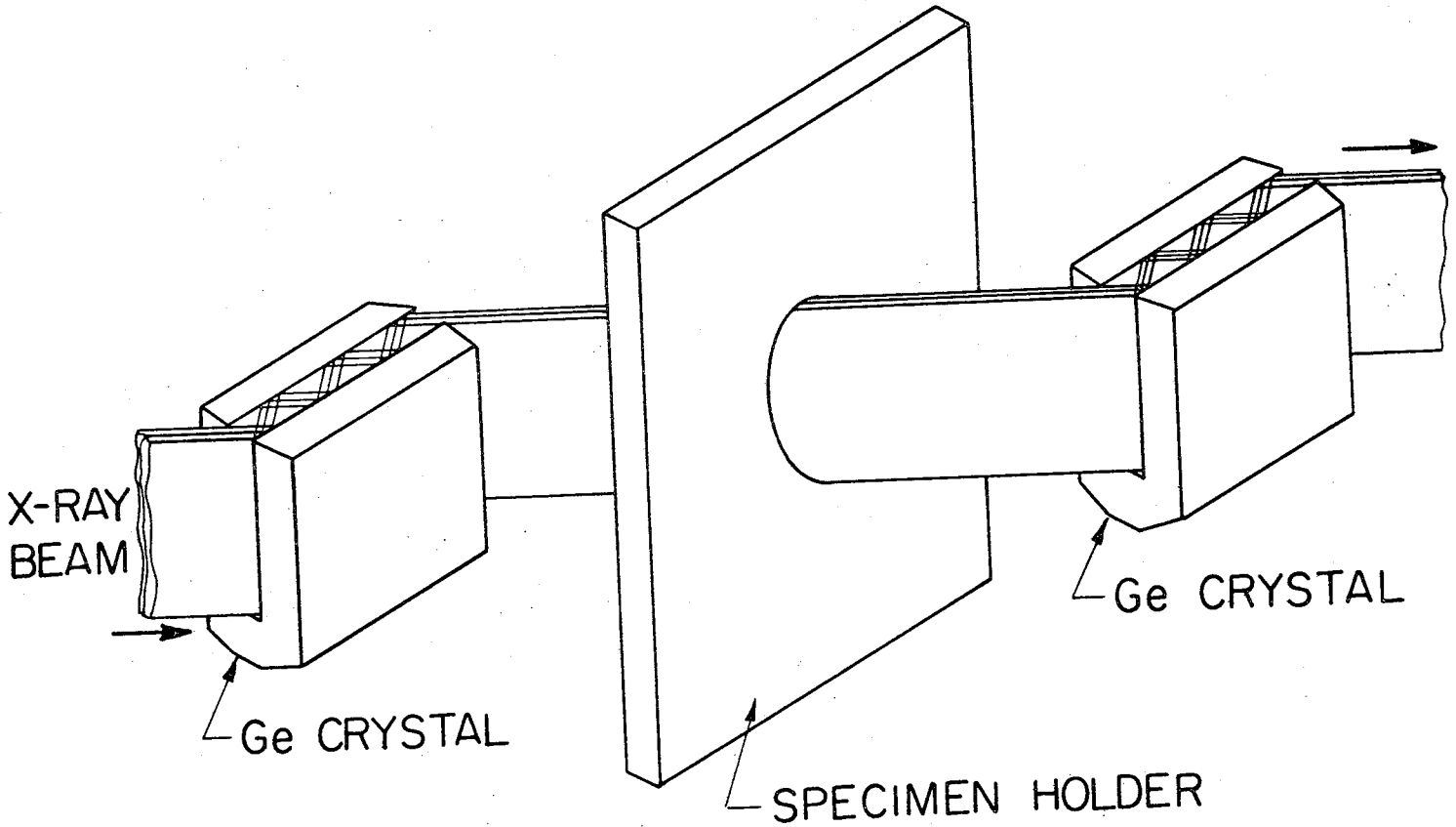

XBL722-6055

Figure 19

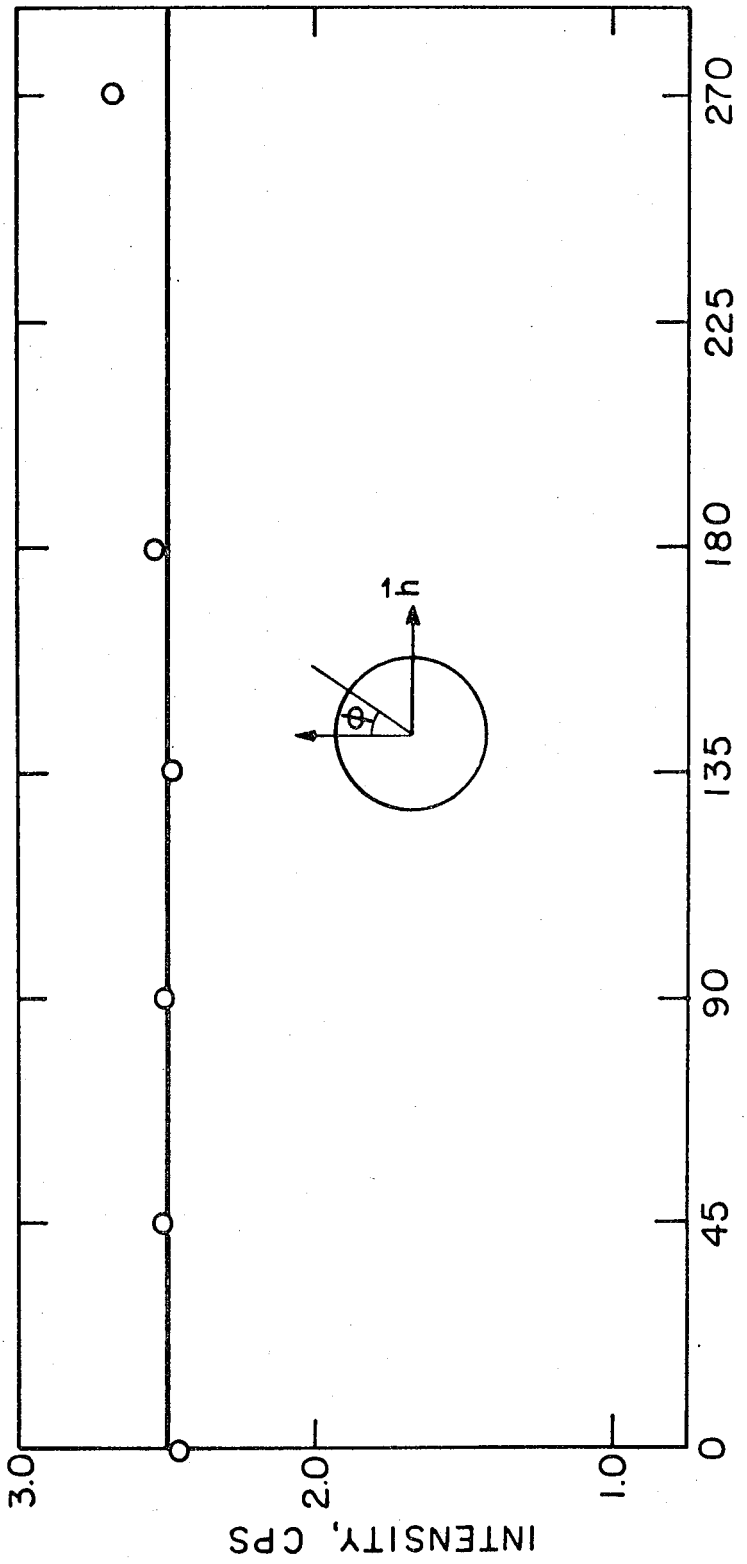

XBL 761-6286

Figure 22

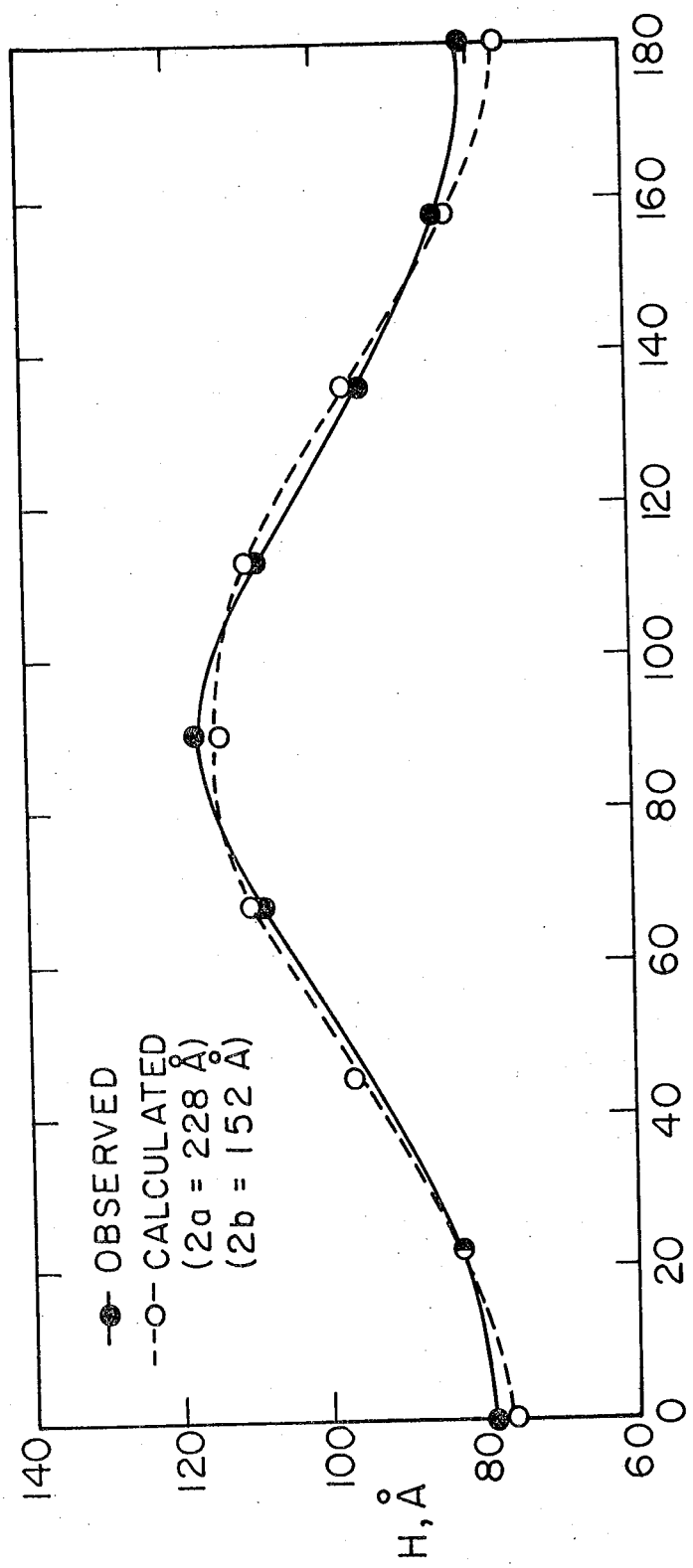
OBSERVED
CALCULATED
(2a = 228 Å)
(2b = 152 Å)
H, Å
140
120
100
80
60
0
20
40
60
80
100
120
140
160
180
γ, DEGREES
XBL 761-6288

Figure 23

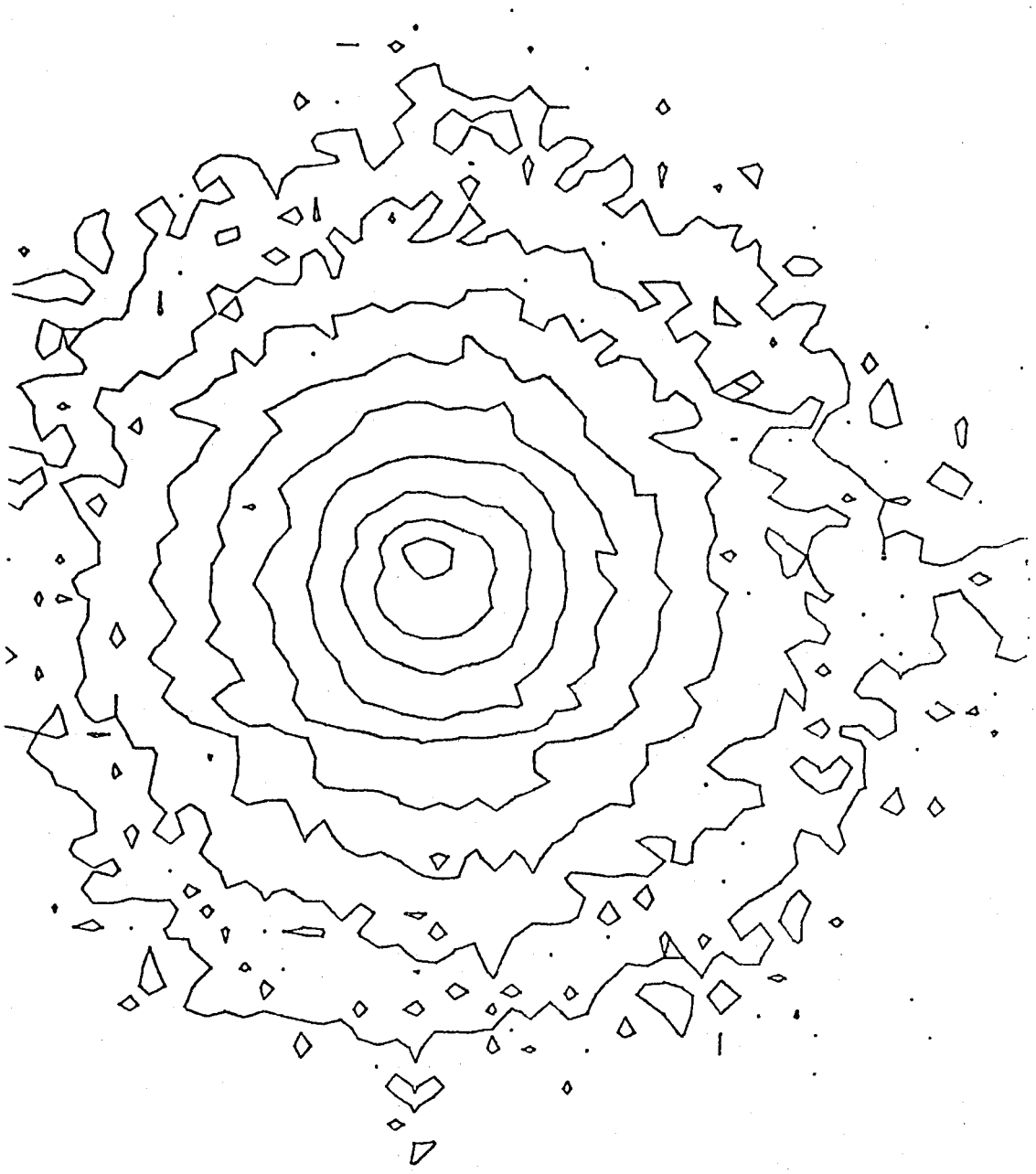

XBL 779-2477

Figure 26

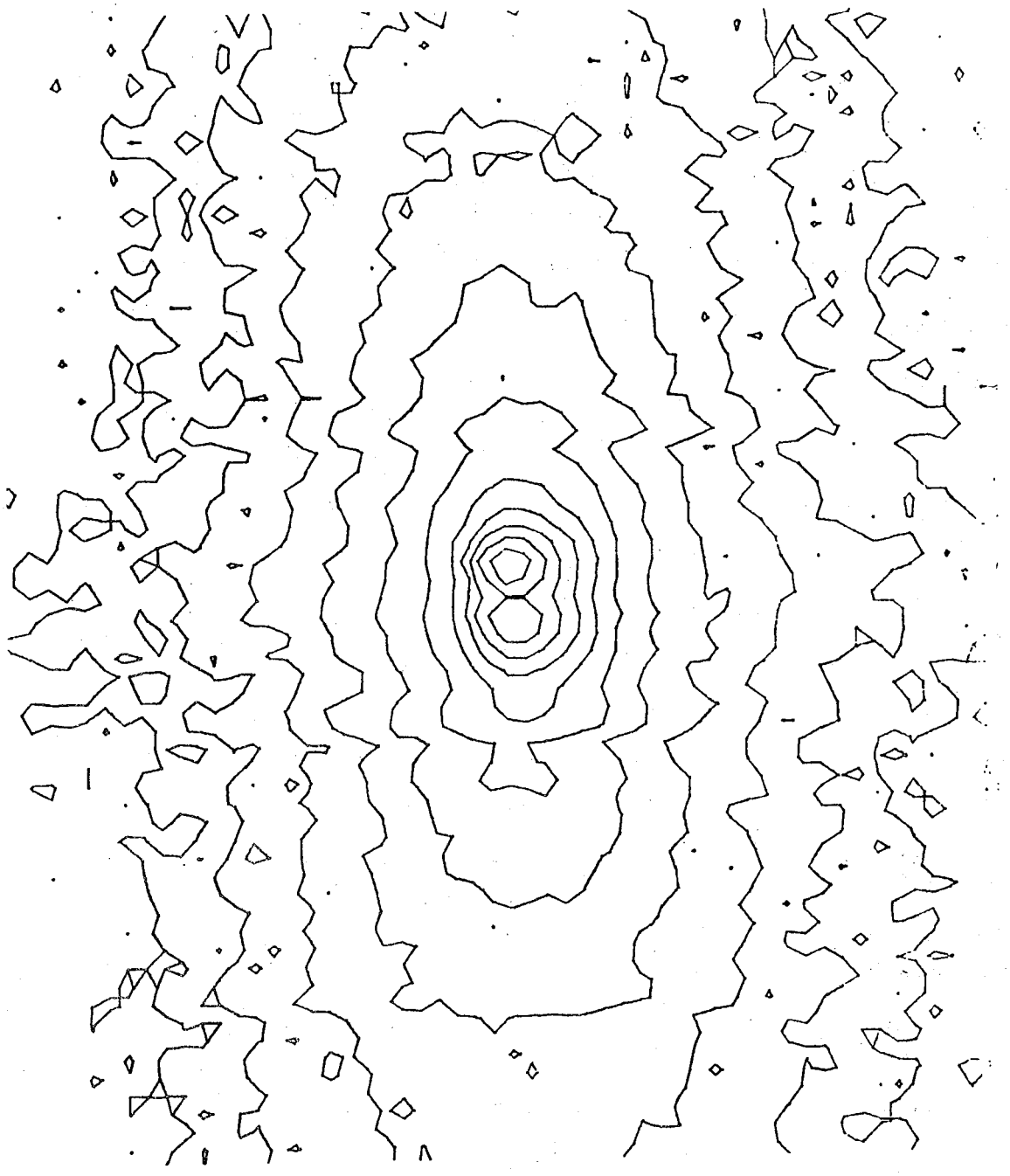

XBL 779-2476

Figure 27

TABLE 1

SC = Single crystal
PC = Polycrystalline

Properties	Graphite	Diamond	GC(2,000)
Density (g/cc)	2.25 (SC) 1.60 (PC)	3.52 (SC)	1.40
Compressive strength (PSI)	8000 (PC)	---	200,000
Tensile strength (PSI)	2000 (PC)	---	25,000
Young's Mod (PSI)	$6X10^6$c (SC) $150X10^6$a (SC) $0.5-3X10^6$(PC)	$114X10^6$	$3.5X10^6$
Thermal Cond cal/cm/^oC/sec	0.19 (PC)	1.5	0.01
Stability	Below 130 kbars	Above 13 kbars	Unstable thermodynamically. Graphitizes above 10 kbars
Thermal exp/^oC	(-) $1.5X10^{-6}$a (SC) $28X10^{-6}$c (SC)	$1.2X10^{-6}$	$5X10^{-6}$
Electrical Cond $(\Omega cm)^{-1}$	3000 a (SC) 0.3 c (SC)	10^{-15}	200
Gas permeability (cm^2/sec)	0.01 (PC)	---	10^{-9}
Bond strength Kcal/mole	in plane 80 normal 4.4	60	---
Unit cell Å	2.46 a 6.71 c hexagonal	3.56	2.5 a 6.9 c
X-ray reflections	if 1 even $h+2k \neq 3(n+1/2)$ if 1 odd $h+2k \neq 3n$	all even or all odd with $h+k+1 = 4n$	hko 001 of graphite

TABLE 2

VARIOUS ACTIVATION ENERGIES FOR GRAPHITE

Mechanism	Energy eV/atom	Reference
Vacancy formation	7.0 ± 0.5	(50)
Interstitial formation	7.5 ± 1.8	(50)
Vacancy migration (a direction)	3.1 ± 0.2	(50)
Vacancy migration (c direction)	> 5.5	(50)
Interstitial migration (a direction)	< 0.1	(50)
Interstitial migration (c direction)	2.8 ± 0.2	(51)
Self diffusion		
Synthetic (bulk)	1.7	(52)
Synthetic (grist)	2.0	(52)
Single crystal	7.2	(53)
Synthetic pile grade	3.5 - 6.5	(54)
Heat of sublimation	7.43	(55)
Graphitization (graphitizable carbon)	11.3	(25)